

## Stellar Characterization and Chemical Abundances of Exoplanet Hosting M dwarfs from APOGEE Spectra: Future JWST Targets

EDYPO MELO,<sup>1</sup> DIOGO SOUTO,<sup>1</sup> KATIA CUNHA,<sup>2,3</sup> VERNE V. SMITH,<sup>4</sup> FÁBIO WANDERLEY,<sup>2</sup> VINICIUS GRILLO,<sup>1</sup> DEUSALETE CAMARA,<sup>1</sup> KELY MURTA,<sup>1</sup> NEDA HEJAZI,<sup>5</sup> IAN J.M. CROSSFIELD,<sup>5</sup> JOHANNA TESKE,<sup>6</sup> RAFAEL LUQUE,<sup>7</sup> MICHAEL ZHANG,<sup>7</sup> AND JACOB BEAN<sup>7</sup>

<sup>1</sup> Departamento de Física, Universidade Federal de Sergipe, Av. Marcelo Deda Chagas, S/N Cep 49.107-230, São Cristóvão, SE, Brazil

<sup>2</sup> Observatório Nacional/MCTIC, R. Gen. José Cristino, 77, 20921-400, Rio de Janeiro, Brazil

<sup>3</sup> Steward Observatory, University of Arizona, 933 North Cherry Avenue, Tucson, AZ 85721-0065, USA

<sup>4</sup> NSF's NOIRLab, 950 N. Cherry Ave. Tucson, AZ 85719 USA

<sup>5</sup> Department of Physics and Astronomy, University of Kansas, Lawrence, KS, USA

<sup>6</sup> Earth & Planets Laboratory, Carnegie Institution for Science, 5241 Broad Branch Road, NW, Washington, DC 20015

<sup>7</sup> Department of Astronomy & Astrophysics, University of Chicago, Chicago, IL, USA

### ABSTRACT

Exoplanets hosting M dwarfs are the best targets to characterize Earth-like or super-Earth planetary atmospheres with the James Webb Space Telescope (JWST). We determine detailed stellar parameters ( $T_{\text{eff}}$ ,  $\log g$ , and  $\xi$ ) and individual abundances of twelve elements for four cool M dwarfs hosting exoplanets TOI-1685, GJ 436, GJ 3470, and TOI-2445, scheduled for future observations by the JWST. The analysis utilizes high-resolution near-infrared spectra from the SDSS-IV APOGEE survey between 1.51–1.69  $\mu\text{m}$ . Based on 1D-LTE plane-parallel models, we find that TOI-2445 is slightly metal-poor ( $[\text{Fe}/\text{H}] = -0.16 \pm 0.09$ ), while TOI-1685, GJ 436 and GJ 3470 are more metal-rich ( $[\text{Fe}/\text{H}] = 0.06 \pm 0.18$ ,  $0.10 \pm 0.20$  dex,  $0.25 \pm 0.15$ ). The derived C/O ratios for TOI-2445, TOI-1685, GJ 436, and GJ 3470 are  $0.526 \pm 0.027$ ,  $0.558 \pm 0.097$ ,  $0.561 \pm 0.029$ , and  $0.638 \pm 0.015$ , respectively. From results for 28 M dwarfs analyzed homogeneously from APOGEE spectra, we find exoplanet-hosting M dwarfs exhibit a C/O abundance ratio approximately 0.01 to 0.05 higher than those with non-detected exoplanets, at limits of a statistically significant offset. A linear regression of  $[\text{Fe}/\text{H}]$  vs. C/O distribution reveals a noticeable difference in the angular coefficient between FGK dwarfs (0.27) and M dwarfs (0.13). Assuming our abundance ratios of Ca/Mg, Si/Mg, Al/Mg, and Fe/Mg, we determine a mass of  $3.276^{+0.448}_{-0.419} M_{\oplus}$  for TOI-2445 b, having density  $(6.793^{+0.005}_{-0.099} \text{ g.cm}^{-3})$  and core mass fraction  $(0.329^{+0.028}_{-0.049})$  very similar to Earth's. We also present an atlas of 113 well-defined spectral lines to analyze M dwarfs in the  $H$ -band and a comprehensive evaluation of uncertainties from variations in the atmospheric parameters, signal-to-noise, and pseudo-continuum.

**Keywords:** Near infrared astronomy(1093) — M dwarf stars(982) — Stellar abundances(1577) — Exoplanets(498)

### 1. INTRODUCTION

M-dwarf stars, characterized by their low masses, small radii, and low effective temperatures ( $T_{\text{eff}}$ ), constitute a substantial portion of the Milky Way's stellar population, accounting for approximately 70% of all stars (Salpeter 1955; Miller & Scalo 1979; Henry et

al. 2018). Despite their prevalence, M dwarfs have remained among the least-studied stellar types regarding their chemical abundances. The intricate optical spectra of M dwarfs, filled with strong molecular bands such as TiO and VO (Allard et al. 2000), have presented significant challenges to unveiling their chemical compositions. An increased interest in studying M dwarf chemical makeup has risen recently, motivated by the growing discovery of Earth-sized exoplanets orbiting these stars and high-resolution instruments operating in the near-

Corresponding author: Edypto Melo  
 edyporibeiro@academico.ufs.br

infrared regime (NIR). The advantageous mass and size ratios between small planets and M dwarfs make Earth-sized-mass exoplanets particularly amenable to detection through radial velocity or transit methods (Charbonneau & Deming 2007; Gaidos et al. 2007; Shields et al. 2016, and Dressing & Charbonneau 2015). This fact, coupled with the need for precise stellar characterization in the star-planet connection, emphasizes the need to improve the methodology for M-dwarf spectral analysis. This is also relevant because exoplanetary atmospheres are key targets for observations by the James Webb Space Telescope (JWST) (Lustig-Yaeger et al. 2023 and May et al. 2023).

The near-infrared (NIR) domain offers an advantageous window for spectroscopic analysis of M dwarf stars, as their spectra are less affected by molecular blends than in the optical range. Within the *H*-band, between 1.51 and 1.69  $\mu\text{m}$ , studies like Souto et al. (2017, 2018, 2020) have used the Apache Point Observatory Galactic Evolution Experiment (APOGEE, Majewski et al. 2017) high-resolution spectrograph ( $R \sim 22,500$ ) and demonstrated the feasibility of determining key atmospheric parameters ( $T_{\text{eff}}$ ,  $\log g$ , metallicity, and micro-turbulence) as well as individual abundances for up to fourteen elements. Additionally, investigations by Birkby et al. (2020), Sarmento et al. (2021) (see also Antoniadis-Karnavas et al. 2020), and others have successfully determined atmospheric parameters for numerous targets using APOGEE spectra, with results aligning well with photometric calibrations and literature findings.

The CARMENES survey, operating in both optical (0.52–0.96 micron) and in the J and H bands at high resolution ( $R \sim 100,000$ ), has contributed to exoplanetary research and M dwarf spectroscopic characterization, finding 33 new planets, confirming 26 planet candidates from transits (Ribas et al. 2023), and characterizing their host star in detail (Reiners et al. 2018; Passegger et al. 2018). Notably, High-Resolution Cross-Correlation Spectroscopy (HRCCS) techniques, as exemplified in works such as Nortmann et al. (2018); Salz et al. (2018); Alonso-Floriano et al. (2019); Sánchez-López et al. (2019), have enabled the determination of abundances in the exoplanetary atmospheres themselves. Using another NIR spectrograph, SPIRou, (Dong et al. 2020), Allart et al. (2019); Pelletier et al. (2021) have probed the atmospheres of exoplanets like WASP-107b and  $\tau$  Boötis b (Allart et al. 2019; Pelletier et al. 2021). Furthermore, the studies by Cristofari et al. (2023) and Wanderley et al. (2024, submitted) determined magnetic fields by analyzing Zeeman splitting in well-defined M dwarf NIR lines. Magnetic fields in M dwarf stars have the potential to generate stellar spots

and inhibit convection in the stellar interior. These effects can lead to an expansion of the stellar radii, causing stellar inflation and reducing its effective temperature (Chabrier et al. 2007). The recent work by Wanderley et al. (2023) investigated radius inflation in M dwarfs belonging to the Hyades open cluster, revealing that, on average, M dwarfs in the Hyades exhibit larger radii than anticipated based on stellar isochrones by about 2%.

This work aims to characterize the atmospheric parameters and chemical abundances of four M dwarf stars hosting exoplanets, TOI-1685, TOI-2445, GJ 436, and GJ 3470. The planets TOI-1685 b and TOI-2445 b were discovered by the Transiting Exoplanet Survey Satellite (TESS) in 2021 (Bluhm et al. 2021) and 2022 (Giacalone et al. 2022), respectively, while the planet GJ 436 b was discovered by Butler et al. (2004) at the W. M. Keck Observatory in 2004, and the planet GJ 3470 b was discovered by Bonfils et al. (2012) using the HARPS spectrograph, located at the La Silla Observatory, in 2012. The detailed analysis and characterization of these planet hosts are of particular interest as their exoplanets are scheduled for observations by JWST.

When we study the chemical composition of a star, we can infer that their respective exoplanets shared the same composition during their formation (although planetary formation processes may significantly alter the exoplanet abundances). The abundance distribution of the cloud that gave birth to the stars and planets plays a critical role in the formation and evolution of planetary systems (Bond et al. 2010; Dorn et al. 2015). For example, the ratio of carbon to oxygen (C/O) in a star plays a crucial role in the chemistry of protoplanetary disks where planets form (Drkačkowska et al. 2023) (see also Nissen 2013, Delgado Mena et al. 2021). A high C/O value can lead to the formation of planets rich in carbonaceous compounds, while a lower value may favor the formation of planets with water-rich atmospheres (Madhusudhan 2012; Teske et al. 2014). The abundance of elements like magnesium, silicon, and iron in a star can influence the composition of an exoplanet's core and mantle (Bond et al. 2010, Delgado Mena et al. 2010, Thiabaud et al. 2015, Dorn et al. 2017, Santos et al. 2017, and Unterborn & Panero 2017). This information is essential for determining whether a planet is predominantly rocky, gaseous, or has an intermediate composition (see Plotynokov & Valencia 2020; Schultze et al. 2020 & 2024). The distribution of these elements in the planet affects its internal structure, density, and, ultimately, its potential to host life as we know it on Earth.

This paper is organized as follows. In Section 2, we present the observations of the four stellar systems scheduled for observations with JWST. Section 3 discusses the details of our data modeling approach. Section 4 presents and discusses the results, including the C/O abundance ratios obtained for the stars. Section 5 provides a summary of our results. Finally, in the Appendix, we evaluate the sensitivity of abundance determinations obtained from *H*-band spectra to variations in stellar parameters, such as  $T_{\text{eff}}$ ,  $\log g$ ,  $\xi$ , and metallicity ( $[\text{Fe}/\text{H}]$ ), as well as the impact that the signal-to-noise ratio (SNR) fluctuations and pseudo-continuum adjustments have on the results.

## 2. OBSERVATIONS

We cross-matched a list of potential exoplanets scheduled for JWST observations<sup>1</sup> with the APOGEE DR17 dataset. This resulted in a total of seventeen stars, seven of which are M dwarfs. Three of these stars exhibit low signal-to-noise ratios (SNR < 20) in DR17, and one presents issues with the reduction as processed by the DR17 APOGEE pipeline. However, its DR 16 (Ahumada et al. 2020) spectrum was found to be of good quality. The remaining four targets, all with high SNR, are analyzed in this study: TOI-1685, GJ 436, TOI-2445, and GJ 3470.

We use observational data collected using the SDSS APOGEE North spectrograph (Wilson et al. 2018). APOGEE is a cryogenic, multi-fiber high-resolution ( $R = 22,500$ ) instrument with 300 fibers in the near-infrared (NIR) spanning a spectral range from 1.51 to 1.69  $\mu\text{m}$  (*H*-band) mounted on a 2.5-meter telescope. This spectrograph was commissioned during the third iteration of the Sloan Digital Sky Survey (SDSS-III) and has been operational at the Apache Point Observatory (APO) in New Mexico, USA, and continues to be used to gather data as part of the Milky Way Mapper Survey (MWM; Kollmeier et al. 2017).

## 3. SPECTRAL LINES AND DATA MODELING

We conduct spectral synthesis to model the APOGEE spectra. Our modeling approach in this study employs 1D plane-parallel LTE MARCS model atmospheres (Gustafsson et al. 2008). For radiative transfer calculations, we use the turbospectrum code (Alvarez & Plez 1998 and Plez 2012), supplemented by the BACHUS wrapper (Masseron et al. 2016) in manual mode for computing the abundances. We adopt a microturbulence velocity equal to 1  $\text{km.s}^{-1}$  as suggested by Souto et al. (2017). Atomic and molecular transition data are

from the APOGEE line list (Smith et al. 2021), which was used to compute the latest SDSS-IV data release (DR17; Abdurro'uf et al. 2022) and, so far, is being utilized in the SDSS-V (Kollmeier et al. 2017).

In this study, we analyze the behavior of 113 spectral lines, focusing on mid to early M dwarfs with effective temperatures between 3200 to 4000K, surface gravity values between 4.5 and 5.5 dex, metallicities spanning from  $[\text{Fe}/\text{H}] = -0.16$  to  $+0.25$  dex, and microturbulent velocities ranging between 0.5 to 1.5  $\text{km.s}^{-1}$ . While most spectral lines are suitable for precise abundance determinations in early-type M dwarfs at  $\sim 3900\text{K}$ , lower effective temperatures result in blending with molecular lines, particularly with  $\text{H}_2\text{O}$  and FeH. In Figure 1, we illustrate the sensitivity of spectral lines to atmospheric parameters within a 70-angstrom window spanning from 15720 to 15790 Å, reflecting the change of lines in both depth and shape due to the variation of these parameters. This particular spectral region is highly responsive to changes in effective temperature, surface gravity, and metallicity, primarily due to the presence of three Mg I lines, marked in Figure 1.

Although the M dwarf stars studied here cover a somewhat narrow range in effective temperature and metallicity (Section 4, Table 3), Table 1 provides a comprehensive list of those 113 well-defined spectral lines suitable for precise individual abundance determinations of M dwarfs in the *H*-band and in particular in the APOGEE region. This table is split into different regimes of  $T_{\text{eff}}$ ; each of the sections in the table indicates the lines available for the respective  $T_{\text{eff}}$  regime. We use these lines to determine the abundances and uncertainties in this work but note that such lines can also be useful for spectral analyses from other high-resolution spectrographs covering the *H*-band, such as CRIRES, CARMENES, and SPIRou, although other well-defined lines might appear as the spectral resolution increases.

## 4. ABUNDANCE ANALYSIS

We examine a set of fourteen elements encompassing transitions from both neutral atomic (Fe I, Na I, Mg I, Al I, Si I, K I, Ca I, Ti I, V I, Cr I, Mn I, Ni I) and molecular lines (CO, OH,  $\text{H}_2\text{O}$ , and FeH). We determined atmospheric parameters,  $T_{\text{eff}}$  and  $\log g$ , by combining  $\text{H}_2\text{O}$  and OH lines, ensuring self-consistent oxygen abundance values. For details of this methodology, we refer to Souto et al. (2020).

Our abundance analysis involves a careful look at each line available (see Table 1) to ensure that only well-defined lines are adopted. From a visual inspection, we remove lines that are either blended, too small, or affected by spectra reduction issues. This is particularly

<sup>1</sup> [www.stsci.edu/~nnikolov/TrExoLiSTS/JWST/trexolists.html](http://www.stsci.edu/~nnikolov/TrExoLiSTS/JWST/trexolists.html).

relevant because as the stellar effective temperature decreases, the water vapor ( $H_2O$ ) and iron hydride lines (FeH) become notably more prominent, often blending those well-defined neutral lines (Allard et al. 2000; Tsuji et al. 2015) in the  $H$ -band spectra of cooler M dwarfs. In this study, the stellar metallicity, [Fe/H], is the average iron abundances derived from Fe I and FeH line indicators.

## 5. RESULTS AND DISCUSSION

The effective temperatures, surface gravity values, metallicities, and individual abundances were calculated using the spectral lines provided in Table 1, and results are summarized in Table 2 and 3. The uncertainties presented in Table 2 were computed by propagating their respective errors in the atmospheric parameters, SNR, and pseudo-continuum change (assumed as 1%) from Tables 4, 5, and 6 via a quadratic sum.

### 5.1. Exoplanet Hosting M dwarfs on JWST targeting list

The search for and characterization of exoplanets are among the most exciting scientific endeavors in modern astronomy. To know an exoplanet well, we need to know its host star well. This is because the chemical composition of stars may play a fundamental role in understanding their exoplanets. Also, knowing the stellar mass, radius, and flux is critical because exoplanet physical properties rely on these parameters (such as  $M_{planet}/M_{star}$ ,  $R_{planet}/R_{star}$ ,  $F_{planet}/F_{star}$ ). Furthermore, the connection between the stars and the planet's chemistry may enable understanding the nature and evolution of exoplanets (Kolecki & Wang 2022; Polanski et al. 2022; Hejazi et al. 2023).

Based on the atmospheric parameters determined in this work, we can use physical relations or calibrations to obtain fundamental stellar properties, such as luminosity, radius, and mass. We determined the absolute magnitudes of the M-dwarfs TOI-1685, GJ 436, TOI-2445, and GJ 3470 using their respective apparent magnitudes from the K band (2MASS; Cutri et al. 2002) and distances from Gaia Collaboration (2022), Bailer-Jones et al. (2021), Stassun et al. (2019), Salz et al. (2015), and Maciejewski et al. (2014). We used the bolometric correction from Mann et al. (2015) to obtain the bolometric magnitude and determine the luminosity from physical relation. We adopt values from Mamajek et al. (2015) of  $M_{bol} = 0.00$ , corresponding to  $L_0 = 3.0128 \cdot 10^{35} \text{ erg s}^{-1}$ , which leads to a solar luminosity of  $3.828 \cdot 10^{33} \text{ erg s}^{-1}$  and  $M_{bol}$  (Sun) = 4.74. We determined the stellar radii

and masses using calibrations from Souto et al. (2020),

$$\frac{R_\star}{R_\odot} = \sum_{n=0}^n a_n (M_{K_S})^n, \quad (1)$$

where  $a_0 = 1.9932$ ,  $a_1 = -0.3659$ , and  $a_2 = 0.0177$ , and  $M_{K_S}$  is the absolute  $K_S$  magnitude. Stellar masses were computed from the equation

$$\frac{M_\star}{M_\odot} = 0.2524 - 0.5765 \left( \frac{R_\star}{R_\odot} \right) + 2.0122 \left( \frac{R_\star}{R_\odot} \right)^2. \quad (2)$$

The adopted photometry and derived stellar masses and radii are presented in Table 3. The internal uncertainty in the derived stellar radii is  $0.03 R_\star/R_\odot$ , while for the derived stellar masses, the internal uncertainty varies from 5 to 10% (about 0.02 to 0.05  $M_\star/M_\odot$ ).

We re-derived the planetary parameters with the stellar parameters derived in this study. We derived the planetary radii of TOI-1685 b, GJ 436 b, TOI-2445 b, and GJ 3470 b from the physical transit equation below,

$$\delta = 1.049 \left( \frac{R_p/R_{Jup}}{R_\star/R_\odot} \right)^2, \quad (3)$$

with transit depths ( $\delta$ ) provided by the Exoplanet Follow-up Observation Program - Transiting Exoplanet Survey Satellite (Ricker et al. 2015) and (Giacalone et al. 2022).

For the determination of planetary masses ( $M_p$ ), we used the radial velocity classical equation (see Torres et al. 2008),

$$M_p \sin i = 4.919 \times 10^{-3} P^{1/3} (1-e^2)^{1/2} K_\star \left( \frac{M_\star + M_p}{M_\odot} \right)^{2/3}, \quad (4)$$

where input parameters are our stellar masses, the planet orbital period ( $P$ ), the radial velocity semi-amplitude ( $K$ ; Kosiarek et al. (2019), Hirano et al. (2021), Rosenthal et al. (2021)), and the eccentricity ( $e$ ; Kosiarek et al. (2019)), Rosenthal et al. (2021)). We assumed the inclination angle ( $i$ ) is  $90^\circ$ .

We also determined the exoplanet equilibrium temperature ( $T_{eq}$ ) from the Stefan-Boltzman physical relation below (see Lissauer & de Pater 2013 for details)

$$T_{eq} = T_{\text{eff}} \sqrt{\frac{R_\star}{2a}} (1 - A_B)^{\frac{1}{4}}, \quad (5)$$

assuming an approximation of no atmosphere and an albedo of 0.306. Table 3 summarizes the exoplanetary parameters adopted in the calculations and those derived in this study. In the following section, we discuss the results for each star-planet system.

**Table 1.** M dwarfs well-defined spectral lines in the *H*-band.

Elements	Lines (in Å)
For $T_{\text{eff}}$ from 4000 K to 3200 K	
Ca	16136.823, 16150.763, 16157.364
K	15163.067, 15168.376
Al	16718.957, 16750.564, 16763.360
Mg	15740.716, 15748.988, 15765.842
Na	16373.853, 16388.858
C	15977.7, 16184.9
$\text{H}_2\text{O}$ (for $T_{\text{eff}} < 3800\text{K}$ )	15256.8, 15258.3, 15258.4, 15259.2, 15259.4, 15270.6, 15315.7, 15317.3, 15317.5, 15353.6, 15360.5 15447.6, 15455.8, 15461.5, 15503.6
For $T_{\text{eff}} = 4000$ K to 3700 K	
Ni	15605.68, 15632.654, 16584.439, 16589.295, 16673.711, 16815.471, 16818.76
Mn	15159.0, 15217.8, 15262.4
Cr	15680.063
V	15924.9
Ti	15334.847, 15543.756, 15602.842, 15698.979, 15715.573, 16635.161
Si	15888.410, 15960.063, 16094.787, 16680.770
OH	15391.208, 15407.288, 15409.308, 15505.782, 15558.023, 15560.244, 15565.961, 15568.780, 15572.084, 16052.765 16055.464, 16061.7, 16065.054, 16069.524, 16074.163, 16190.263, 16192.208, 16204.076, 16207.186, 16352.217 16354.582, 16364.590, 16368.135, 16581.250, 16582.013, 16866.688, 16871.895, 16879.090, 16884.530, 16886.279 16895.180, 16898.887
FeI	15207.5, 15219.5, 15244.8, 15294.6, 15395, 15490.3, 15591.8, 15604, 15621.7, 15632
FeH	15648.5, 15662, 15692.5, 15723.5 15965, 16009.6, 16018.5, 16108.1, 16114, 16245.7, 16271.8, 16284.7, 16299.4, 16377.4 16546.8, 16548.8, 16557.2, 16574.8, 16694.4, 16735.4, 16738.3, 16741.7, 16796.4, 16812.7 16814.1, 16889.6, 16892.9, 16922.7, 16935.1
For $T_{\text{eff}} = 3600$ K	
Mn	15159
V	15924.9
Ti	15334.847, 15543.756, 15715.573
Si	15888.410
OH	15391.208, 15407.288, 15409.308, 15505.782, 15558.023, 15560.244, 15565.961, 15568.780, 15572.084, 16052.765 16055.464, 16061.7, 16065.054, 16069.524, 16074.163, 16190.263, 16192.208, 16204.076, 16207.186, 16352.217 16354.582, 16364.590, 16368.135, 16581.250, 16582.013, 16866.688, 16871.895, 16879.090, 16884.530, 16886.279 16895.180, 16898.887
FeI	15207.5, 15219.5, 15294.6, 15621.7, 15632, 15723.5
FeH	15965, 16009.6, 16018.5, 16108.1, 16114, 16245.7, 16271.8, 16284.7, 16299.4, 16377.4 16546.8, 16548.8, 16557.2, 16574.8, 16889.6, 16892.9, 16935.1
For $T_{\text{eff}} = 3500$ K	
Mn	15159
V	15924.9
Ti	15334.847, 15543.756, 15715.573
Si	15888.410
OH	15391.208, 15407.288, 15409.308, 15505.782, 15558.023, 15560.244, 15565.961, 15568.780, 15572.084, 16052.765 16055.464, 16061.7, 16065.054, 16069.524, 16074.163, 16190.263, 16192.208, 16204.076, 16207.186, 16352.217 16354.582, 16364.590, 16368.135, 16581.250, 16582.013, 16866.688, 16871.895, 16879.090, 16884.530, 16886.279 16895.180, 16898.887
FeI	15207.5, 15219.5, 15294.6, 15621.7, 15632, 15723.5
FeH	15965, 16009.6, 16018.5, 16108.1, 16114, 16245.7, 16271.8, 16284.7, 16299.4, 16377.4 16546.8, 16548.8, 16557.2, 16574.8, 16889.6, 16892.9, 16935.1
For $T_{\text{eff}} = 3400$ K	
Ti	15334.847, 15543.756, 15715.573
Si	15888.410
OH	15391.208, 15407.288, 15409.308, 15505.782, 15558.023, 15560.244, 15565.961, 15568.780, 15572.084, 16052.765 16055.464, 16061.7, 16065.054, 16069.524, 16074.163, 16190.263, 16192.208, 16204.076, 16207.186, 16352.217 16354.582, 16364.590, 16368.135, 16581.250, 16582.013, 16866.688, 16871.895, 16879.090, 16884.530, 16886.279 16895.180, 16898.887
FeI	15207.5, 15219.5, 15294.6, 15621.7, 15632, 15723.5
FeH	15965, 16009.6, 16018.5, 16108.1, 16114, 16245.7, 16271.8, 16284.7, 16299.4, 16377.4 16546.8, 16548.8, 16557.2, 16574.8, 16889.6, 16892.9, 16935.1
For $T_{\text{eff}} = 3300$ K	
Ti	15334.847, 15543.756, 15715.573
Si	15888.410
OH	15391.208, 15407.288, 15409.308, 15505.782, 15558.023, 15560.244, 15565.961, 15568.780, 15572.084, 16052.765 16055.464, 16061.7, 16065.054, 16069.524, 16074.163, 16190.263, 16192.208, 16204.076, 16207.186, 16352.217 16354.582, 16364.590, 16368.135, 16581.250, 16582.013, 16866.688, 16871.895, 16879.090, 16884.530, 16886.279 16895.180, 16898.887
FeI	15207.5, 15219.5, 15294.6, 15621.7, 15632, 15723.5
FeH	15965, 16009.6, 16018.5, 16108.1, 16114, 16245.7, 16271.8, 16284.7, 16299.4, 16377.4 16546.8, 16548.8, 16557.2, 16574.8, 16889.6, 16892.9, 16935.1
For $T_{\text{eff}} = 3200$ K	
Ti	15334.847, 15543.756, 15715.573
Si	15888.410
OH	15391.208, 15407.288, 15409.308, 15505.782, 15558.023, 15560.244, 15565.961, 15568.780, 15572.084, 16052.765 16055.464, 16061.7, 16065.054, 16069.524, 16074.163, 16190.263, 16192.208, 16204.076, 16207.186, 16352.217 16354.582, 16364.590, 16368.135, 16581.250, 16582.013, 16866.688, 16871.895, 16879.090, 16884.530, 16886.279 16895.180, 16898.887
FeI	15207.5, 15219.5, 15294.6, 15621.7, 15632, 15723.5
FeH	15965, 16009.6, 16018.5, 16108.1, 16114, 16245.7, 16271.8, 16284.7, 16299.4, 16377.4 16546.8, 16548.8, 16557.2, 16574.8, 16889.6, 16892.9, 16935.1

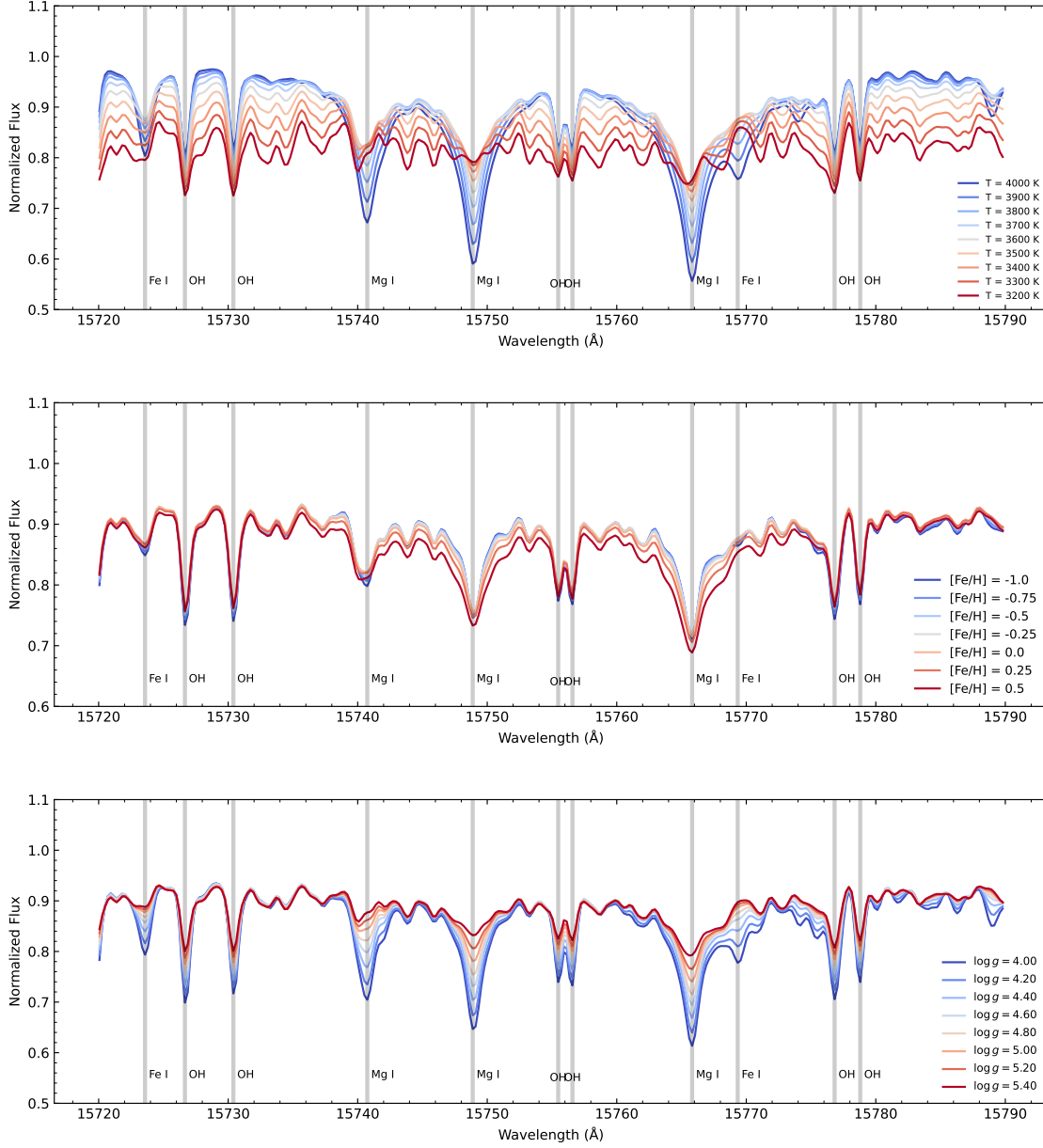


**Figure 1.** Sensitivity to variations in stellar atmospheric parameters. Top panel: spectral synthesis varying  $T_{\text{eff}}$  from 3200K (redder line) to 4000K (bluer line) in steps of 100K with fixed values of  $\log g$  (4.8 dex),  $[\text{Fe}/\text{H}]$  (0.00 dex), and  $\xi$  ( $1.00 \text{ km.s}^{-1}$ ). Middle panel: spectral synthesis varying  $[\text{Fe}/\text{H}]$  from 0.5 (redder line) to -1.0 (bluer line) in steps of 0.25 dex with fixed values of  $T_{\text{eff}}$  (3500K),  $\log g$  (4.8 dex), and  $\xi$  ( $1.00 \text{ km.s}^{-1}$ ). Bottom panel: spectral synthesis varying  $\log g$  from 5.4 (redder line) to 4.0 (bluer line) in steps of 0.2 dex with fixed values of  $T_{\text{eff}}$  (3500K),  $[\text{Fe}/\text{H}]$  (0.00 dex), and  $\xi$  ( $1.00 \text{ km.s}^{-1}$ ).

**Table 2.** Abundances of exoplanet Hosting M dwarfs on JWST targeting list.

Element	TOI-1685	GJ 436	TOI-2445	GJ 3470
[Fe/H]	0.06±0.178	0.10±0.199	-0.16±0.094	0.25±0.152
[C/Fe]	-0.15±0.108	-0.07±0.146	0.08±0.110	-0.05±0.104
[O/Fe]	-0.12±0.093	-0.05±0.093	0.13±0.098	-0.08±0.097
[Na/Fe]	0.03±0.118	–	–	-0.03±0.120
[Mg/Fe]	-0.05±0.172	0.00±0.178	0.01±0.144	-0.07±0.159
[Al/Fe]	-0.10±0.095	0.00±0.100	-0.05±0.084	-0.16±0.097
[Si/Fe]	-0.11±0.235	0.01±0.264	–	-0.05±0.206
[K/Fe]	-0.03±0.063	-0.11±0.075	-0.04±0.083	-0.16±0.057
[Ca/Fe]	0.04±0.083	-0.03±0.090	0.06±0.121	0.00±0.074
[Ti/Fe]	-0.26±0.084	-0.20±0.089	-0.25±0.101	-0.26±0.088
[V/Fe]	-0.18±0.250	–	–	-0.09±0.183
[Mn/Fe]	0.00±0.040	0.04±0.167	–	-0.08±0.133
C/O	0.558±0.027	0.561±0.097	0.526±0.029	0.638±0.015

### 5.1.1. TOI-1685

TOI-1685 (2MASS J04342248+4302148, TIC 28900646) is an M dwarf star located 37.6 parsecs away from our Sun (Gaia Collaboration 2022), having a spectral type M3.0 V, and belonging to the thin disk of our Galaxy (Bluhm et al. 2021). We determine TOI-1685 to have a  $T_{\text{eff}}$  of  $3519\pm100$ K and  $\log g$  of  $4.63\pm0.13$  dex, and our effective temperature is slightly hotter but in agreement, within the uncertainties, with the results from Bluhm et al. (2021) of  $T_{\text{eff}}=3434\pm51$ K and  $\log g=4.85\pm0.04$  dex. The latter study measured stellar parameters and metallicities from the stacked CARMENES VIS spectra and from fits to a synthetic grid of PHOENIX-SESAM models (Husser et al. 2013, Pasquegger et al. 2019). Our derived radius and mass are  $0.453\pm0.014R_{\odot}$  and  $0.405\pm0.041M_{\odot}$ , respectively, while the previous work by Bluhm et al. (2021) derived a mass of  $0.495\pm0.019M_{\odot}$ , and a radius of  $0.492\pm0.015R_{\odot}$  for TOI-1685.

TOI-1685 exhibits a moderate rotation rate for being an early M dwarf. Our best fit synthetic spectrum for this star was obtained for a rotational velocity ( $v \sin i$ ) of  $7.0 \text{ km.s}^{-1}$ , which is close to the threshold  $v \sin i$  that can be measured using APOGEE spectra. Concerning stellar activity, this star exhibits a pseudo-equivalent width, pEW(H $\alpha$ ), of  $+0.51 \text{ \AA}$ , which is indicative of it being active (Cincunegui et al. 2007), but it exhibits

a lack of X-ray and ultraviolet emission. Its estimated age is in the range between 0.6 and 2 Gyr, based on gyrochronology relations and comparisons with open clusters like Praesepe (Kraus & Hillenbrand 2007).

We derived a near-solar metallicity for TOI-1685 of  $[\text{Fe}/\text{H}] = 0.06\pm0.18$  dex. The previously mentioned study by Bluhm et al. (2021) found this star to be more metal-poor  $[\text{Fe}/\text{H}] = -0.13\pm0.16$ , while Hirano et al. (2021) reported a higher metallicity of  $[\text{Fe}/\text{H}] = 0.14\pm0.12$  dex from a weighted average of the TRES spectra analysis by specMatch-Emp (Yee et al. 2017), the InfraRed Doppler (IRD) spectra (Ishikawa et al. 2020), and SED fitting with the NextGen model. Besides being observed by the APOGEE survey, TOI-1685 was also observed by the LAMOST survey, with reported metallicities in APOGEE DR17 of -0.05 (Abdurro'uf et al. 2022) and LAMOST DR2 of -0.20 dex (Ding et al. 2022). It has been previously shown from APOGEE studies of M dwarfs in the Coma Berenice (Souto et al. 2021) and Hyades (Wanderley et al. 2023) open clusters that the metallicities obtained by the APOGEE pipeline for cooler M dwarfs in DR 17 are systematically lower than expected. Here, for TOI-1685, we find a  $\sim 0.1$  dex difference with the metallicity in DR17, a similar result within the uncertainties. The discrepancy with the metallicity from LAMOST possibly highlights the challenges in accurately determining metallicities for low-mass stars at low resolution ( $R \sim 1900$ ).

Hirano et al. (2021) work also reported abundances for seven elements, including Na, Mg, Si, Ca, Ti, and Mn.

**Table 3.** Stellar and exoplanetary parameters.

	TOI-1685 (b)	GJ 436 (b)	TOI-2445 (b)	GJ 3470 (b)
Stellar parameters				
$M_k$	5.882	6.127	7.347	5.646
$BC_k$	2.689	2.694	2.718	2.673
$M_{bol}$	8.571	8.821	10.065	8.318
$L/L_\odot$	0.029	0.023	0.007	0.037
$R/R_\odot$	$0.453 \pm 0.014$	$0.416 \pm 0.013$	$0.260 \pm 0.08$	$0.492 \pm 0.015$
$M/M_\odot$	$0.405 \pm 0.041$	$0.361 \pm 0.036$	$0.239 \pm 0.024$	$0.455 \pm 0.046$
$T_{\text{eff}} (K)$	$3519 \pm 100$	$3507 \pm 100$	$3318 \pm 100$	$3640 \pm 100$
$\log g$	$4.63 \pm 0.13$	$4.81 \pm 0.13$	$4.94 \pm 0.13$	$4.79 \pm 0.13$
distance (pc)	37.60	9.75	48.58	29.42
V	13.378	10.670	15.692	12.332
J	9.616	6.900	11.555	8.794
H	9.005	6.319	11.033	8.206
K	8.758	6.073	10.779	7.989
Exoplanetary parameters				
Transit Depth ( $\delta$ %)	0.102	0.691	0.182	0.569
Semi Major axis ( $a$ au)	0.012	0.029	0.006	0.036
Period ( $P$ days)	0.669	2.644	0.371	3.337
Radial velocity amplitude ( $K$ m.s $^{-1}$ )	4.200	17.120	–	8.210
Eccentricity ( $e$ )	–	0.145	–	0.114
$R/R_\oplus$	$1.759 \pm 0.010$	$3.645 \pm 0.018$	$1.375 \pm 0.005$	$4.352 \pm 0.028$
$M/M_\oplus$	$3.142 \pm 0.807$	$18.548 \pm 0.405$	$3.276 \pm 0.434^\dagger$	$11.276 \pm 0.497$
$T_{\text{eq}} (K)$	$979 \pm 28$	$583 \pm 17$	$936 \pm 28$	$592 \pm 16$

$^\dagger$  Mass computed with ExoPlex (Unterborn & Panero 2017).

We find good agreement in Na and Ca abundances ( $\delta$  this work - Hirano et al. 2021)  $< 0.10$  dex). However, our results for Mg, Si, and Mn show a systematic difference, with Hirano et al. (2021) reporting higher values, up to 0.50 dex. The largest difference is observed for Ti (0.83 dex), where Hirano et al. (2021) results appear to be notably higher.

TOI-1685 hosts at least one planet: TOI-1685 b, whose transits, eclipses, and thermal phase curve are being observed by JWST in GO programs 3263, 4098, and 4195 (Luque et al. 2023; Benneke et al. 2023; Fisher et al. 2023). It was discovered in 2021 using the transit method with the TESS satellite (Ricker et al. 2015). This planet is a “super-Earth” orbiting TOI-1685 at a close distance, just 0.012 astronomical units (AU) away from the star (Hirano et al. 2021), and it completes one orbital period in 0.669 days (Luque & Pallé 2022). Our results for the mass and radius of TOI-1685 b are of  $3.142 \pm 0.81 M_\oplus$  and  $1.759 \pm 0.01 R_\oplus$ , respectively, and this compares well with previous results from the literature (Luque & Pallé 2022) obtained a mass of

$3.09 \pm 0.58 M_\oplus$  and a radius of about  $1.70 R_\oplus$ ). TOI-1685 b boasts a high density of  $4.122 \text{ g.cm}^{-3}$ , about 75% of Earth’s density (Luque & Pallé 2022). Compared to our Solar System, TOI-1685 b is significantly more massive than the Earth, larger in radius, and denser than Mars. Its proximity to its star resembles Mercury’s distance from the Sun.

With the semi-major axis of the orbit provided in Hirano et al. (2021) and the effective temperature and stellar radius from this study, we obtain an equilibrium temperature for TOI-1685 b of  $979 \pm 28 K$ . The literature results for the equilibrium temperature for this planet are overall slightly higher than ours. The equilibrium temperature obtained by Bluhm et al. (2021) is  $1069 \pm 16 K$ , and that obtained by Hirano et al. (2021) is  $1052 \pm 26 K$ . We note, however, that our determination does not account for any atmosphere or greenhouse effect and that we assume an Earth-like albedo.

### 5.1.2. GJ 436

Gliese 436 (GJ 436; J11421096+2642251) is a  $M2.5V$  star situated 9.75 parsecs away from the Sun (Salz et al. 2015, Maciejewski et al. 2014). GJ 436 has a mass of  $M=0.47M_{\odot}$  and a radius of  $R=0.45R_{\odot}$  (Maciejewski et al. 2014). Rosenthal et al. (2021) derives an effective temperature of  $3586K$ , while Bourrier et al. (2018) report  $T_{\text{eff}}$  of  $3479 \pm 60K$ . Our determination for  $T_{\text{eff}}$  falls between these two studies, with  $T_{\text{eff}}=3507 \pm 100K$ , while we derive  $\log g$  of  $4.81 \pm 0.13\text{dex}$ . Our results for the stellar radius and mass are  $R=0.417 \pm 0.013R_{\odot}$  and  $M=0.362 \pm 0.036M_{\odot}$ , respectively. Our analysis reveals that GJ 436 is slightly metal-rich, with  $[\text{Fe}/\text{H}] = +0.10 \pm 0.20$ . Using CARMENES spectra, Schweitzer et al. (2019) find GJ 436 metallicity to be  $[\text{Fe}/\text{H}] = -0.04 \pm 0.16$ , which is slightly more metal-poor than ours.

Comparing our findings with those of Ishikawa et al. (2022), who also determined abundances for Fe, Mg, Si, K, Ca, Ti, and Mn using IRD spectra, we find good overall agreement within the uncertainties. The difference in  $[\text{Fe}/\text{H}]$  between our work and theirs is 0.02 dex. For Si, K, Ca, and Mn, the difference is less than 0.07 dex, indicating close agreement. However, we observe larger discrepancies for Mg and Ti, with differences of -0.18 and -0.41 dex, respectively. Additionally, our results align with those of Maldonado et al. (2020), who utilized high-resolution optical spectra from HARPS-N to determine abundances for seven elements overlapping with our study: Fe, C, Mg, Al, Si, Ca, Ti, and Mn. The difference in  $[\text{Fe}/\text{H}]$  between our study and theirs is -0.09 dex. Notably, the difference for Al is -0.03 dex, while for Si, it is 0.01 dex. However, variations are more pronounced for C, Ti, Mn, Mg, and Ca, with differences of -0.11 dex, -0.13 dex, 0.09 dex, 0.21 dex, and 0.29 dex, respectively.

GJ 436 hosts at least one exoplanet, GJ 436 b, which was observed in secondary eclipse by the JWST GTO programs 1177 and 1185 (Greene et al. 2017, and Greene et al. 2017). GJ 436 b is the prototypical exo-Neptune, as it was the first planet discovered with a size and mass comparable to Neptune:  $R=4.17 \pm 0.17R_{\oplus}$ , with a mass that is approximately 22.1 times that of Earth (Butler et al. 2004, Gillon et al. 2007). The orbital semi-major axis of GJ 436 b is  $a=0.029$  AU, with a period of  $P=2.644$  days (Maciejewski et al. 2014). Our determinations for the planetary radius and mass are  $R=3.645 \pm 0.018R_{\oplus}$  and  $M=18.606M_{\oplus}$ .

The planet has been subjected to atmospheric characterization via transit, eclipse, and thermal phase measurements from numerous observatories (Stevenson et al. 2010). These results suggest that the planetary atmosphere is substantially deficient in methane relative to expectations from equilibrium chemistry and a solar-

like, hydrogen-rich composition at the planet's expected temperature; the atmosphere is likely either significantly metal-rich ( $\gtrsim 300 \times$  solar) and/or exhibits substantial disequilibrium chemistry (Stevenson et al. 2010; Moses et al. 2013; Morley et al. 2017). Using the orbital semi-major axis from Maciejewski et al. (2014), along with our effective temperature and stellar radius, we obtain an equilibrium temperature of GJ 436 b of  $583 \pm 17K$ , while Turner et al. (2016) report a somewhat higher value of  $686 \pm 10K$ .

The mystery deepens as the planet is too compact to be primarily composed of hydrogen gas, similar to gas giants like Jupiter. Yet, it is not compact enough to be classified as a rocky super-Earth, having a density of  $1.80 \pm 0.29 \text{ g.cm}^{-3}$  (Maciejewski et al. 2014). One of the hypotheses regarding the composition of GJ 436 b suggests that it might predominantly consist of an exotic form of solid water. This unique water phase is believed to have solidified due to extreme pressure rather than low temperatures (Gillon et al. 2007). This well-known degeneracy in interpreting masses and radii of exo-Neptunes makes it difficult to identify the bulk composition of the planet from mass and radius alone (Adams et al. 2008, Figueira et al. 2009). Only spectroscopy of the exoplanet can hope to reveal its atmospheric composition unambiguously.

### 5.1.3. TOI-2445

TOI-2445 (J02531581+0003087) is an M dwarf situated at a distance of approximately 48.58 parsecs, with a mass of  $M=0.25M_{\odot}$  and a radius of  $R=0.27R_{\odot}$  (Giacalone et al. 2022). According to Giacalone et al. (2022), TOI-2445 has  $T_{\text{eff}}=3333 \pm 157K$ , while our determination for the effective temperature is  $3318 \pm 100K$ , in very good agreement. We obtain  $\log g=4.94 \pm 0.13$  dex, while our results for the star's mass and radius are  $M=0.240 \pm 0.024M_{\odot}$  and  $R=0.262 \pm 0.08R_{\odot}$ , respectively.

This star hosts at least one known exoplanet, TOI-2445 b, that is categorized as a super-Earth, while JWST is observing its transit, eclipse, and phase curve in GO program 3784 (Zhang et al. 2023). Concerning its physical characteristics, TOI-2445 b has a mass of about  $2.0M_{\oplus}$  and a radius of  $1.25 \pm 0.08 R_{\oplus}$  (Giacalone et al. 2022). Orbiting at only 0.006 AU, TOI-2445 b has an orbital period of 0.371 days. Due to its small orbital radius, TOI-2445 b is subjected to intense irradiation, creating an extreme environment. TOI-2445 b's orbital eccentricity is assumed to be 0.0 (Morello et al. 2023) and using the semi-major axis of the orbit provided by Giacalone et al. (2022), along with our results for the star's effective temperature and radius, we find

a planetary equilibrium temperature of  $936 \pm 28 K$ , while [Giacalone et al. \(2022\)](#) calculated a slightly higher equilibrium temperature of  $1060 \pm 54 K$ . In addition, we determined a planetary radius of  $1.375 \pm 0.005 R_{\oplus}$ , slightly higher than that presented in the literature.

TOI-2445 has very few metallicity studies in the literature, with APOGEE and LAMOST reporting values of  $-0.44$  and  $-0.54$  dex, respectively. Our analysis yields  $[Fe/H] = -0.16 \pm 0.094$  dex, indicating a slightly sub-solar metallicity. This value is larger by  $\sim +0.3$  to  $+0.4$  dex from those obtained by APOGEE and LAMOST. This metallicity difference for such a cool M dwarf is not surprising. As discussed earlier in Section 4.1.1, the APOGEE DR 17 pipeline abundances are systematically lower (by about this same amount) than those derived from the spectroscopic analyses of [Souto et al. \(2021\)](#) and [Wanderley et al. \(2023\)](#). The similar discrepancy with the LAMOST metallicity likely results from the difficulties in measuring chemical abundances in cool M dwarfs from low-resolution optical spectra. Using IRD spectra, [Morello et al. 2023](#) derived consistent metallicity values from spectral synthesis ( $[M/H] = -0.32 \pm 0.07$ ), and SED fitting ( $[M/H] = -0.34 \pm 0.07$ ) for TOI-2445. These values are located between our results and those from APOGEE and LAMOST.

TOI-2445 b's mass has not been observationally derived because it has yet to be confirmed via radial velocity (or by any other exoplanet discovery method). However, by assuming the exoplanet shares the same abundance ratios as its host star, we can determine the mass of TOI-2445 b using the ExoPlex code, an open-source mass-radius-composition solver. ExoPlex calculates a planetary mass or radius based on its bulk composition of Mg, Si, Al, Ca, and Fe ([Unterborn & Panero 2017](#)). The input parameters are our derived exoplanetary radius ( $1.375 \pm 0.005 R_{\oplus}$ ), along with our abundance ratios of  $Ca/Mg = 0.0638$ ,  $Al/Mg = 0.0756$ , and  $Fe/Mg = 0.8958$ . We were not able to determine a Si abundance for TOI-2445. Therefore, we adopt an alpha-elemental abundance as a proxy for Si, where  $[Si/Fe] \sim [(O+Mg+Ca)/3Fe]$ , in which we obtain  $Si/Mg = 0.9016$ . From these parameters, ExoPlex reports TOI-2445 b has a mass of  $3.276^{+0.448}_{-0.419}$  Earth masses. The errors are estimated by propagating the uncertainties in our derived abundances and those from the exoplanetary radius. We find our mass determination of TOI-2445 b to be similar, within the uncertainties, to the one derived from [Giacalone et al. \(2022\)](#) using an estimate of the semi-amplitude of the radial velocity (RV) signal for this planet of  $K_{RV} = 4.5^{+2.8}_{-1.7} \text{ m.s}^{-1}$ , which corresponds to a  $M_p = 2.0^{+1.2}_{-0.7} M_{\oplus}$ . The density of TOI-2445 b is  $6.793^{+0.005}_{-0.099} \text{ g.cm}^{-3}$ , indicating the planet is likely to be

composed of a rocky (Fe+Ni) core. Assuming [Zeng et al. \(2016\)](#) planetary density curves, we obtain TOI-2445 b to be at a very similar density distribution as the Earth, with a rock-dominated internal structure.

The proportions of a planet's core and mantle depend on complex factors, such as the amount of iron compared to the other constituent elements and the oxidation state of the core and the mantle. In ExoPlex, the ratios that most significantly contribute to a planet's core mass fraction are Fe/Mg and Si/Mg. Consequently, variations in these abundances result in a range of values for the core mass fraction, directly affecting the planetary mass and surface gravity. In the case of TOI-2445 b, we obtain a core mass fraction of  $32.85^{+0.028}_{-0.049}$ , which is very similar to the Earth's (0.33) within the uncertainties. This modeling is consistent with what is expected, given the variations in Si/Mg and Fe/Mg abundances between the Earth and TOI-2445 b.

#### 5.1.4. GJ 3470

Gliese 3470 is an M dwarf located at a distance of approximately 29.42 pc ([Bonfils et al. 2012](#)). Our results for the stellar parameters and metallicity of GJ 3470 are  $T_{\text{eff}} = 3640 \pm 100 \text{ K}$ ,  $\log g = 4.79 \pm 0.13 \text{ dex}$ , and  $[Fe/H] = +0.25 \pm 0.15 \text{ dex}$ . The results in the literature for this star agree very well with our determination. According to [Awiphan et al. \(2016\)](#), GJ 3470 has  $T_{\text{eff}} = 3600 \pm 100 \text{ K}$ ,  $\log g = 4.695 \pm 0.046 \text{ dex}$ , and  $[Fe/H] = +0.20 \pm 0.10 \text{ dex}$ , and [Kosiarek et al. \(2019\)](#) reports  $T_{\text{eff}} = 3652 \pm 50 \text{ K}$ ,  $\log g = 4.658 \pm 0.035 \text{ dex}$ , and the same value for metallicity. The stellar mass obtained in this study for GJ 3470 was  $0.455 \pm 0.046 M_{\odot}$ , whereas for the stellar radius, our result is  $0.492 \pm 0.015 R_{\odot}$ . As a comparison, [Awiphan et al. \(2016\)](#) determine  $M_{\star} = 0.539 \pm 0.045 M_{\odot}$  and  $R_{\star} = 0.547 \pm 0.018 R_{\odot}$ .

GJ 3470 hosts at least one exoplanet, GJ 3470 b ([Bonfils et al. 2012](#)). The Neptune-like planet is located at 0.036 AU from its star, with an orbital period of approximately 3.337 days ([Awiphan et al. 2016](#)). The analysis of GJ 3470 b from [Kosiarek et al. \(2019\)](#), presents an equilibrium temperature of  $615 \pm 16 \text{ K}$ , with values for mass and radius of  $12.58^{+1.31}_{-1.28} M_{\oplus}$  and  $3.88 \pm 0.32 R_{\oplus}$ , respectively.

Using the semi-major axis of the orbit provided by [Awiphan et al. \(2016\)](#) and our determination for the effective temperature and stellar radius, the calculated equilibrium temperature for the exoplanet is  $592 \pm 16 \text{ K}$ . Finally, the exoplanetary radius obtained is  $4.352 \pm 0.028 R_{\oplus}$ , in addition to a planet mass of  $11.276 \pm 0.497 M_{\oplus}$ .

The low density of GJ 3470 b would support the presence of an atmosphere dominated by H<sub>2</sub> ([Biddle](#)

et al. 2014). Fukui et al. (2013) and Nascimbeni et al. (2013) observed wavelength-dependent variations in transit depths, indicating changes in atmospheric opacity. It is important to emphasize that Fukui et al. (2013) argued that GJ 3470 b would not have a thick layer of clouds. On the other hand, in the K-band, Crossfield et al. (2013) detected a flat transmission spectrum, implying a hazy, low-methane, and/or metal-rich atmosphere. Nascimbeni et al. (2013) found a difference in transit depth between ultraviolet and optical wavelengths, suggesting a Rayleigh-scattering slope consistent with a hazy atmosphere. Lastly, Bourrier et al. (2018) determined the presence of an extensive exosphere of neutral hydrogen around the planet. Using HST/WFC3 and *Spitzer* transits and eclipses, Benneke et al. (2019) reported an atmosphere with  $\text{H}_2\text{O}$  absorption, revealing low-to-moderate metallicity —  $\text{O/H} = 0.2\text{--}18.0$  relative to Solar — and scattering clouds.

### 5.2. The $\text{El}/\text{Fe}$ abundance ratios

The metallicities of the four planet-hosting stars in this study range from slightly metal-poor ( $[\text{Fe}/\text{H}] = -0.16$ ) to metal-rich ( $[\text{Fe}/\text{H}] = +0.25$ ). Their measured  $[\text{el}/\text{Fe}]$  ratios for the studied elements Na, Mg, Al, Si, K, Ca, Ti, V, and Mn (Table 2) generally overlap with previous  $[\text{El}/\text{Fe}]$  vs  $[\text{Fe}/\text{H}]$  results for benchmark M dwarf stars from the studies of Souto et al. (2022) and the chemical evolution of these elements in the restricted range in metallicity of the sample stars (see figure 6 and 7 from Souto et al. 2022). The abundance ratio of C/O will be discussed next.

### 5.3. The C/O abundance ratio

The C/O ratio can influence the availability of carbon and oxygen within exoplanet atmospheres, potentially causing them to become predominantly incorporated into molecules such as  $\text{CH}_4$ ,  $\text{H}_2\text{O}$ , and CO. This phenomenon makes the carbon and oxygen content diagnostic of (and fundamentally shaping) the exoplanet temperature structure and composition (Madhusudhan 2012; Teske et al. 2014). Similarly, the ratio of volatiles such as C and O to S has also been suggested as a complementary diagnostic of a planet’s formation location and accretion history (Pacetti et al. 2022; Schneider & Bitsch 2021; Crossfield 2023). Unfortunately, the S I lines are either blended or too weak to be properly studied for M dwarf stars in the APOGEE wavelength.

For the four studied stars, we obtain  $\text{C/O} = 0.558 \pm 0.027$  for TOI-1685,  $\text{C/O} = 0.526 \pm 0.029$  for TOI-2445,  $\text{C/O} = 0.561 \pm 0.097$  for GJ 436, and for GJ 3470 the C/O is  $0.638 \pm 0.015$  (Table 2). We find that our C/O abundance ratio is smaller than solar for

three stars and higher for the most metal-rich star, GJ 3470. The solar value reference adopted is from Asplund et al. (2021), where  $\text{C/O} = 0.589$ .

In Figure 2, we show the C/O ratio distribution as a function of metallicity for the four JWST targets studied here, along with other M dwarfs studied by Souto et al. (2017), Souto et al. (2018), Souto et al. (2020), which used the same analysis methodology as in this study. The orange circles represent the studied stars (all having detected exoplanets); orange triangles are M dwarfs studied by Souto et al. with exoplanets detected, while the gray squares are M dwarfs from Souto et al. without exoplanets detected so far. We also present in this figure the C/O vs.  $[\text{Fe}/\text{H}]$  of exoplanet hosting FGK dwarfs from Nissen (2013) (green triangles), stars from Teske et al. (2014) (with detected exoplanets shown as a light blue diamond), and from Delgado Mena et al. (2021) (with detected exoplanets represented by a pink circle, and without detected exoplanets as a yellow cross).

To explore C/O trends as a function of metallicity for hosting and non-hosting exoplanets, we display four curves representing the linear regressions of the  $[\text{Fe}/\text{H}]$  vs. C/O distribution for M dwarfs with planet detected (solid orange line), M dwarfs without planet detected (solid gray line), FGK dwarfs with planet detected (dashed orange line), and FGK dwarfs without planet detected (dashed gray line). We find no clear distinction or offset between the regressions for FGK dwarfs (with/without exoplanet detected to date) besides an intersection and in the metallicity about -0.20. However, an offset is observed in the distribution of M dwarfs with and without exoplanets detected to date. The C/O ratio for M dwarfs hosting exoplanets is consistently higher by 0.01 to 0.05 dex compared to those without detected exoplanets. This difference is particularly pronounced in the metal-poor regime. Given that the typical uncertainty in our C/O measurement is about 0.03 (see Table 2), this offset resides at the limits of a statistically significant claim that exoplanets hosting M dwarfs display a systematic higher C/O abundance ratio.

We note that there is a distinct angular coefficient in the linear regression of the  $[\text{Fe}/\text{H}]$  vs. C/O distribution for M dwarfs compared to FGK dwarfs. The slope for FGK dwarfs ( $\sim 0.27$ ) is roughly double that observed for M dwarfs ( $\sim 0.14$ ). Interestingly, there is no significant difference in slope when comparing the C/O distribution with and without detected exoplanets. As discussed in Souto et al. (2020), elemental abundance results for M dwarfs (obtained using the same methodology as here) and those for FGK stars from optical studies in the literature for wide-binary systems featuring a warmer primary and a secondary M dwarf showed no discernible

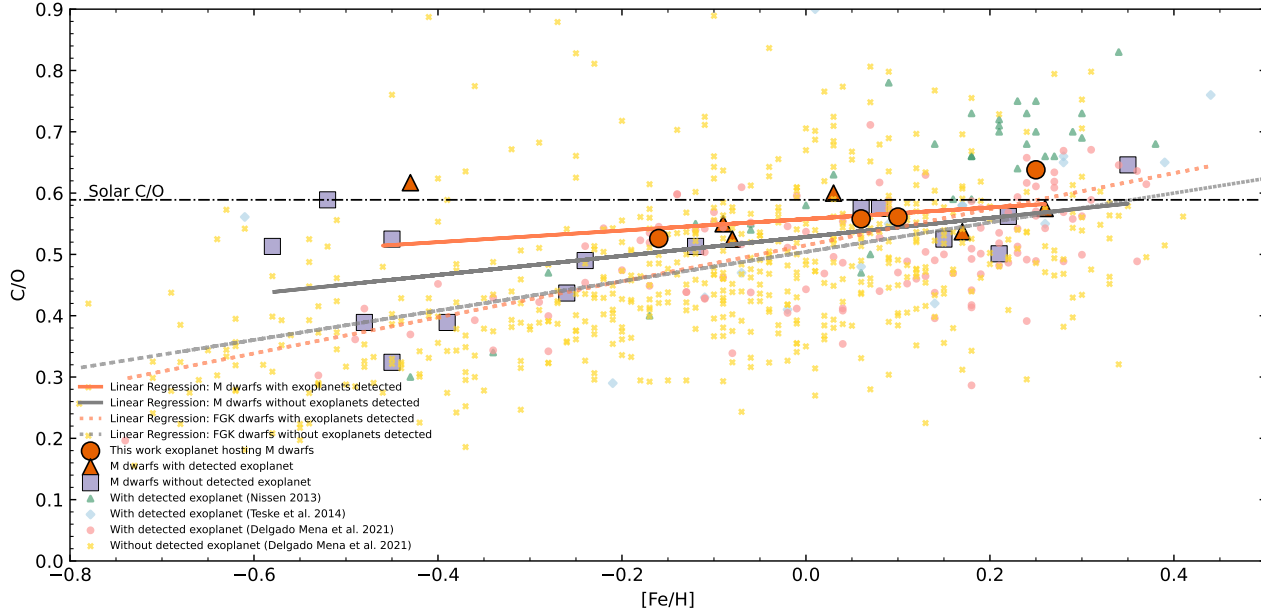


**Figure 2.** The  $[Fe/H]$  versus C/O distribution for this work sample, as well as other M dwarfs studied by Souto et al. (2017), Souto et al. (2018), Souto et al. (2020). The orange circles represent the results for the four JWST targets studied here; Results for M dwarfs from our previous studies (all based on the same methodology as here) are also shown: orange triangles are M dwarfs with exoplanets detected, while the gray squares are M dwarfs without exoplanets detected so far. We also present results for FGK dwarfs from Nissen (2013) (green triangles; all with detected exoplanets), Teske et al. (2014) with (light blue diamonds) detected exoplanets, and Delgado Mena et al. (2021) with (pink circles), and without detected exoplanets (yellow cross). Additionally, four curves represent the linear regressions of the  $[Fe/H]$  vs. C/O distribution for M dwarfs with planet detected (solid orange line), M dwarfs without planet detected (solid gray line), FGK dwarfs with detected planets (dashed orange line), and FGK dwarfs without detected planets (dashed gray line).

systematic offset between the abundances. This substantiates the likelihood that the shallower slope observed in the M dwarf C/O vs.  $[Fe/H]$  distribution is a genuine signature.

One possible physical explanation for the offset in the C/O distribution could be attributed to the atomic diffusion process, which depletes abundances in FG dwarfs, particularly intensifying as stellar metallicity decreases (Souto et al., 2018, 2019, 2021; Dotter, 2017). However, when studying abundance ratios like C/O, we anticipate that atomic diffusion signatures may be mitigated due to their similar intensity across different elements. Other contributing factors may include variations in age distribution or the transient nature of many M dwarfs in the solar neighborhood, possibly originating from different regions of our galaxy. This is supported by the observation that a significant portion of M dwarfs within 100 pc of the Sun exhibit higher proper motions compared to AFG dwarfs (RECONS catalog; [www.recons.org](http://www.recons.org)). In future investigations, we aim to explore potential correlations between these variations and physical processes in Galactic chemical evolution.

## 6. SUMMARY

We conducted a detailed spectroscopic analysis, using SDSS APOGEE  $H$ -band spectra, for four M-dwarf stars, TOI-1685, GJ 436, TOI-2445, and GJ 3470. These stars host Earth-like or Neptune-like exoplanets and are scheduled for observation by JWST. Accurate spectroscopic characterization of the stellar parameters and individual abundances is crucial for enhancing the precision of transmission spectroscopic observations of their associated exoplanets. Notably, our spectral analysis did not reveal any significant Zeeman split lines, which would suggest, in principle, that potential interference from starspots or stellar activity during exoplanet transits may be minimal.

We followed the same analysis methodology discussed in our previous works Souto et al. (2020) to derive stellar effective temperatures and surface gravities from a spectral synthesis of water and OH lines present in the APOGEE spectra. The derived sample has effective temperatures in the range between  $\sim 3300$  -  $3600$  K and  $\log g$  between  $\sim 4.6$  -  $4.9$ . We also derived stellar masses and radii for the sample using calibrations from our previous work Souto et al. (2020), resulting in stellar radii ranging from  $0.262$  to  $0.492 R_{\odot}$ , and stellar masses ranging from  $0.240$  to  $0.455 M_{\odot}$ .

Planetary masses and radii were also derived for the studied sample using the stellar parameters from this work. Using equation 3, we find that TOI-1685 b, GJ 436 b, TOI-2445 b, and GJ 3470 b have  $R/R_{\oplus}$  of 1.759, 3.659, 1.385, and 4.352. Using equation 4, we find that and for TOI-1685 b, GJ 436 b, and GJ 3470 b have masses of  $M/M_{\oplus}$  of 3.142, 18.606, and 11.276, respectively.

The metallicities obtained from the four planet-hosting M dwarf stars range from slightly metal-poor to metal-rich. For TOI-1685, we obtained a near-solar metallicity, with  $[Fe/H]=0.06\pm0.18$  dex. In the case of GJ 436, we measured a relatively higher iron abundance of  $[Fe/H]=0.10\pm0.20$  dex, while for TOI-2445, we derived a sub-solar metallicity of  $[Fe/H]=-0.16\pm0.094$  dex. Finally, our analysis indicated that GJ 3470 is the most metal-rich star, with  $[Fe/H]=0.25\pm0.15$ . The measured abundance ratios of  $[Na/], [Mg/], [Al/], [Si/], [K/], [Ca/], [Ti/], [V/], [Mn/Fe]$  in the four stars generally overlapped with the chemical evolution of these elements in the Galactic disk within the restricted range in the metallicity of the sample stars.

Based on our derived abundance ratios of  $Ca/Mg$ ,  $Si/Mg$ ,  $Al/Mg$ , and  $Fe/Mg$ , we determined a mass of  $3.276^{+0.448}_{-0.419} M_{\oplus}$  for TOI-2445 b, and a density of  $6.793^{+0.005}_{-0.099} \text{ g.cm}^{-3}$ , having a rock-dominated internal structure likely similar to the Earth (core mass fraction of  $0.329^{+0.028}_{-0.049}$ ).

To constrain the chemical properties of the protoplanetary disks that gave rise to these exoplanets, we determined the fundamental carbon-to-oxygen (C/O) ratios for the exoplanet-hosting M dwarfs in this small sample, revealing C/O ratios of  $0.558\pm0.027$  for TOI-1685,  $0.526\pm0.029$  for TOI-2445,  $0.561\pm0.097$  for GJ 436, and  $0.638\pm0.015$  for GJ 3470. These C/O ratios (for four M dwarfs), when combined with our previous abundance analyses of M dwarfs in Souto et al. (2017, 2018, 2020), yield a sample of 28 M dwarfs whose values for C/O were derived from homogeneous analyses of APOGEE spectra. The results from this combined sample of M dwarfs, which consists of both exoplanet hosting and non-hosting stars, reveal a consistent trend among the M dwarfs, where the C/O ratios for exoplanet-hosting stars are consistently higher, by about 0.01 to 0.05, when compared to M dwarfs without detected exoplanets (Figure 2). This offset is not observed for FGK dwarfs. This result could suggest that among M dwarfs, a protoplanetary disk richer in carbon relative to oxygen is more likely to form super-Earth or mini-Neptune exoplanets. Also, we find that the linear regression from the  $[Fe/H]$  vs. C/O distribution reveals a notable difference in the angular coefficient for M dwarfs compared

to FGK dwarfs. FGK dwarfs exhibit a slope of approximately 0.27, roughly twice that of M dwarfs, which show a slope of around 0.13. In addition, there is no significant difference in slope when comparing the C/O distribution with and without detected exoplanets for the FGKM dwarfs.

Finally, this paper presents (in an appendix) an uncertainty atlas for the abundances of M dwarfs with effective temperatures between 3200 - 4000 K, obtained from computed spectra between  $1.5 - 1.7 \mu\text{m}$ , compiling abundance sensitivities and uncertainties stemming from atmospheric parameter ( $T_{\text{eff}}$ ,  $\log g$ ,  $[Fe/H]$ ,  $\xi$ ) variations, SNR, and pseudo-continuum placements. This atlas can enable a more realistic estimation of abundance uncertainties for M dwarf stars studied in the  $H$ -band.

We thank the referee for suggestions that helped improve the paper. D.S. thanks the National Council for Scientific and Technological Development – CNPq. N.H. acknowledges support from NSF AAG grant No. 2108686, and from NASA ICAR grant No. NNH19ZDA001N. R.L. acknowledges funding from University of La Laguna through the Margarita Salas Fellowship from the Spanish Ministry of Universities ref. UNI/551/2021-May 26, and under the EU Next Generation funds. This study was financed in part by the Coordenação de Aperfeiçoamento de Pessoal de Nível Superior – Brasil (CAPES) – Finance Code 001.

Funding for the Sloan Digital Sky Survey IV has been provided by the Alfred P. Sloan Foundation, the U.S. Department of Energy Office of Science, and the Participating Institutions. SDSS-IV acknowledges support and resources from the Center for High-Performance Computing at the University of Utah. The SDSS website is [www.sdss.org](http://www.sdss.org). SDSS-IV is managed by the Astrophysical Research consortium for the Participating Institutions of the SDSS Collaboration including the Brazilian Participation Group, the Carnegie Institution for Science, Carnegie Mellon University, the Chilean Participation Group, the French Participation Group, Harvard-Smithsonian Center for Astrophysics, Instituto de Astrofísica de Canarias, The Johns Hopkins University, Kavli Institute for the Physics and Mathematics of the Universe (IPMU) / University of Tokyo, Lawrence Berkeley National Laboratory, Leibniz Institut für Astrophysik Potsdam (AIP), Max-Planck-Institut für Astronomie (MPIA Heidelberg), Max-Planck-Institut für Astrophysik (MPA Garching), Max-Planck-Institut für Extraterrestrische Physik (MPE), National Astronomical Observatory of China, New Mexico State University, New York University, University of Notre Dame, Observatório Nacional / MCTI, The Ohio State University, Pennsylvania State University, Shanghai Astronomical Observatory, United Kingdom Participation Group, Universidad Nacional Autónoma de México, University of Arizona, University of Colorado Boulder, University of Oxford, University of Portsmouth, University of Utah, University of Virginia, University of Washington, University of Wisconsin, Vanderbilt University, and Yale University.

*Facility:* Sloan Digital Sky Survey (SDSS-IV)

*Software:* Turbospectrum (Alvarez & Plez 1998, Plez 2012), MARCS ([Gustafsson et al. 2008](#)), Bacchus ([Masseron et al. 2016](#)), ExoPlex ([Unterborn & Panero 2017](#)), Matplotlib ([Hunter 2007](#)), Numpy ([van der Walt et al. 2011](#)), RECONS catalog; [www.recons.org](http://www.recons.org).

## APPENDIX

### A. AN UNCERTAINTY ATLAS IN M DWARF *H*-BAND SPECTRA

Abundance determinations are based on modeling the stellar atmospheres, which involves understanding how radiation interacts with a star’s outer layers, and the precision of these models plays a vital role in the accuracy of abundance calculations. Any uncertainties in the stellar parameters, such as effective temperature, surface gravity ( $\log g$ ), and microturbulence ( $\xi$ ), directly affect abundance estimates. Departures from local thermodynamic equilibrium (non-LTE effects) can also affect the line strengths and shapes and introduce additional complexities into the analyses. In addition, spectroscopic observations are not immune to instrumental and observational errors. Variability in telescope performance, detector sensitivity, and data reduction techniques can introduce systematic errors. These errors can be particularly challenging to quantify accurately. In addition to systematic uncertainties, abundance determinations also involve random errors. These errors are associated with the inherent randomness in observations and measurements. They can include statistical fluctuations and variations due to atmospheric, instrumental, and/or line selection conditions. Consequently, noise and measurement errors may affect abundance determinations. In particular, weak lines are more susceptible to these sources of uncertainty than stronger lines.

This appendix presents the uncertainties in the derived abundances but also provides an uncertainty atlas based on the sensitivities of the abundances for baseline models with effective temperatures varying from 3200 - 3900 K in steps of 100 K. Our analysis of the uncertainties encompasses changes in atmospheric parameters ( $T_{\text{eff}}$ ,  $\log g$ , [Fe/H], and microturbulence), pseudo-continuum location, and signal-to-noise ratios. The selected wavelength and resolution range are based on the capability of the APOGEE spectrograph (but can be extended for higher-resolution studies), which is widely used for M dwarf characterization and is integral to the SDSS-V MWM survey. Additional sources of uncertainty in our abundance analysis were not extensively addressed in this study, as they are generally expected to have a smaller impact than atmospheric parameter variations, SNR, and pseudo-continuum displacements. For instance, blends resulting from H<sub>2</sub>O and FeH opacities, as observed in Figure 1, can contribute to pseudo-continuum depletion and potentially affect other elemental abundances. However, previous work by [Souto et al. \(2017\)](#) suggests that their influence is minor.

#### A.1. *Uncertainties due to changes in the Atmospheric parameters*

Variations in  $T_{\text{eff}}$  (Figure 1 top panel) span from 4000 to 3200K in regular increments of 100K (color-coded from blue to red in the Figure). As  $T_{\text{eff}}$  decreases, the spectral lines become less prominent, presenting challenges for analysis, a trend we observe in other wavelengths in the *H*-band as well. Among the displayed lines, the Mg I lines exhibit the highest sensitivity to changes in  $T_{\text{eff}}$ , while the depth of OH lines remains relatively constant at approximately 0.75 in normalized synthetic spectra. Notably, this panel highlights the presence of a pseudo-continuum depletion. As  $T_{\text{eff}}$  decreases, the opacity of H<sub>2</sub>O transitions intensifies, leading to continuum suppression. This effect becomes more pronounced below 3500K, resulting in a typical depletion of approximately 15 to 20% from the continuum. It’s worth noting that this depletion introduces significant uncertainties related to the pseudo-continuum definition (refer to Section A.3).

For Figure 1 middle panel, we vary model metallicity from  $-1.0$  to  $0.5$  at regular intervals of  $0.25$  dex, keeping all abundances constant at the solar scale. We assume the  $T_{\text{eff}}$  fixed at 3500K, while surface gravity remains at 4.80 dex. We observe a difference in the line profile much smaller than changing  $T_{\text{eff}}$ . The Mg I lines are more sensitive to model metallicity variations, whereas the OH lines’ depth remains relatively unchanged. Additionally, the continuum shows no significant variation across the different ranges of model metallicity studied. In Figure 1 bottom panel, we present synthesis with changes in  $\log g$  ranging from  $4.0$  to  $5.4$  dex at regular intervals of  $0.20$  dex. The effective temperature and metallicity are fixed at 3500K and solar value, respectively. We note that lower values for surface gravity are linked to deeper spectral lines, which gradually smooth out as this atmospheric parameter increases with higher  $\log g$  values. It is related to increasing internal pressure and higher rates of collisional broadening in the line formation. The behavior is similar for all species in the window and is reminiscent of the entire *H*-band spectra.

We initially constructed a spectral synthesis grid (assumed to match APOGEE resolution) with fixed atmospheric parameter values to assess the impact of errors in abundance measurements due to atmospheric parameter uncertainties. This grid is, therefore, interpreted as our simulated observed spectra. Subsequently, we calculate individual

abundances based on these simulated spectra. Next, we systematically vary the model atmosphere parameters: effective temperature by  $\pm 100$  K and  $\pm 50$  K,  $\log g$  and [Fe/H] by  $\pm 0.20$  and  $\pm 0.10$  dex, and microturbulence velocity by  $\pm 0.50$  and  $\pm 0.25$  km.s $^{-1}$ . We then recompute the corresponding abundances, assuming these changes in the model atmosphere. The discrepancy between the abundances obtained from the synthesis grid and those resulting from the variation in atmospheric parameters defines our typical uncertainty attributable to changes in atmospheric parameters ( $\sigma_{AP}$ ).

In Table 4, we display the abundance sensitivities as a function of changes in stellar atmospheric parameters. The elements we study are Fe (from Fe I and FeH lines), C (from CO lines), O (from OH and H<sub>2</sub>O lines), and the elements Na, Mg, Al, Si, K, Ca, Ti, V, Cr, Mn, and Ni, all from neutral lines. The sensitivity analysis adopts baseline models with effective temperature values ranging from 3900K to 3200K at regular intervals of 100K. We expect these respective abundance sensitivity shifts to be linear (presented in Table 4), and we can interpolate them whether necessary to obtain an abundance sensitivity for a different set of uncertainties in the atmospheric parameters. It's worth noting that as the reference effective temperatures decrease, some spectral lines become impractical to investigate properly due to molecular blends. This is why there are gaps in Table 4. Chromium and Nickel already become impractical for analysis at effective temperatures of about 3600 K. Vanadium and Manganese, on the other hand, become unfeasible for investigation only from effective temperatures of around 3400K.

The elements Mg and Si are the ones displaying the highest abundance sensitive to changes in  $T_{\text{eff}}$  ( $\gtrsim 0.20$  dex), followed by Fe (from FeI lines), O (from H<sub>2</sub>O lines), and Al ( $\sim 0.10$  dex). The ones showing less abundance sensitivity to  $T_{\text{eff}}$  are C and O (from OH lines) ( $\lesssim 0.03$  dex). Regarding changes in  $\log g$ , Mg, Si, and Fe (Fe I) are the most responsive, with variations of approximately 0.15 dex. On the other hand, C and O (H<sub>2</sub>O) exhibit lower sensitivity to  $\log g$ . The abundance sensitivity to changes in metallicity is relatively consistent across all elements. O (from H<sub>2</sub>O lines), Na and Fe (from FeH lines) are typically the most sensitive, with changes exceeding 0.10 dex. Abundance deviations from changes in microturbulence velocity are minimal for all elements, typically staying below 0.03 dex.

### A.2. Uncertainties due to changes in the signal-to-noise ratio

The signal-to-noise per pixel ratio (SNR) is a measure used to assess the quality or strength of a signal in relation to the background noise level. A higher SNR indicates a stronger, more reliable signal than the noise, making it easier to detect and analyze the data. In general, high-resolution stellar spectroscopy assumes SNR > 60 – 100 (Jofré et al. 2019) to be enough to determine individual abundances precisely. In this paper case, we will validate these for M dwarfs in the *H*-band.

We apply a normal random distribution (using the Python library Numpy) to introduce noise into our spectral synthesis. Therefore, we obtain a synthesis with a controlled degree of noise where we assume them as our “observed spectra”. Subsequently, we add noise levels ranging from SNR of 40 to 300 in steps of 20, and we apply this noise for all ranges of  $T_{\text{eff}}$  adopted in this work ( $T_{\text{eff}}$  of 3200 to 4000K, in 100K steps). We assume fix values of  $\log g = 4.80$  dex, [Fe/H] = 0.00 dex, and  $\xi = 1.00$  km.s $^{-1}$  in this case.

The noise added accounts for a random variation of each pixel in our spectral synthesis. To obtain the abundance uncertainty relative to changes in SNR, we then create a total of 20 syntheses for each set of atmospheric parameters ( $T_{\text{eff}}$ ,  $\log g$ ,  $\xi$ , and [Fe/H]) and SNR analyzed, and compute their respective elemental abundances. We assume the SNR uncertainty ( $\sigma_{\text{SNR}}$ ) to be the standard deviation of the mean of the abundances derived from these 20 random “observed spectra”. We adopt a number of 20 interactions because both mean and standard deviation reach a stable plateau, obviating the necessity for further iterations.

In Table 5, we provide an overview of uncertainties related to changes in SNR. As our highest SNR value studied is 300, we assume higher SNR stars to have the same abundance uncertainties as those with SNR = 300. Figure 3 illustrates the relationship between SNR and uncertainty ( $\sigma$ ), with each element along with the set of the studied  $T_{\text{eff}}$ 's represented in separate panels. As expected, the figure demonstrates a general trend of decreasing standard deviation of the mean ( $\sigma_{\text{SNR}}$ ) as SNR increases. Regarding sensitivity to  $T_{\text{eff}}$ , we typically observe higher uncertainties at fixed SNR values for lower  $T_{\text{eff}}$ . Notably, FeH and OH lines consistently exhibit uncertainties below 0.05 dex, owing to their numerous well-defined lines (refer to Table 1). The same is true for K I lines, but only two lines are available in the APOGEE wavelength coverage. Similar trends, with slightly higher uncertainties for SNR < 100, are observed for H<sub>2</sub>O, Al, K, Ca, Ti, and Mn. For Fe (Fe I lines), CO, Mg, V, and Ni, the uncertainty remains around 0.05 dex when SNR exceeds 200. However, lower SNR values, such as SNR = 40 for cool stars, can lead to uncertainties exceeding 0.15 dex. Notably, Na and Si exhibit higher uncertainties due to changes in SNR. Even at SNR = 300, the uncertainty

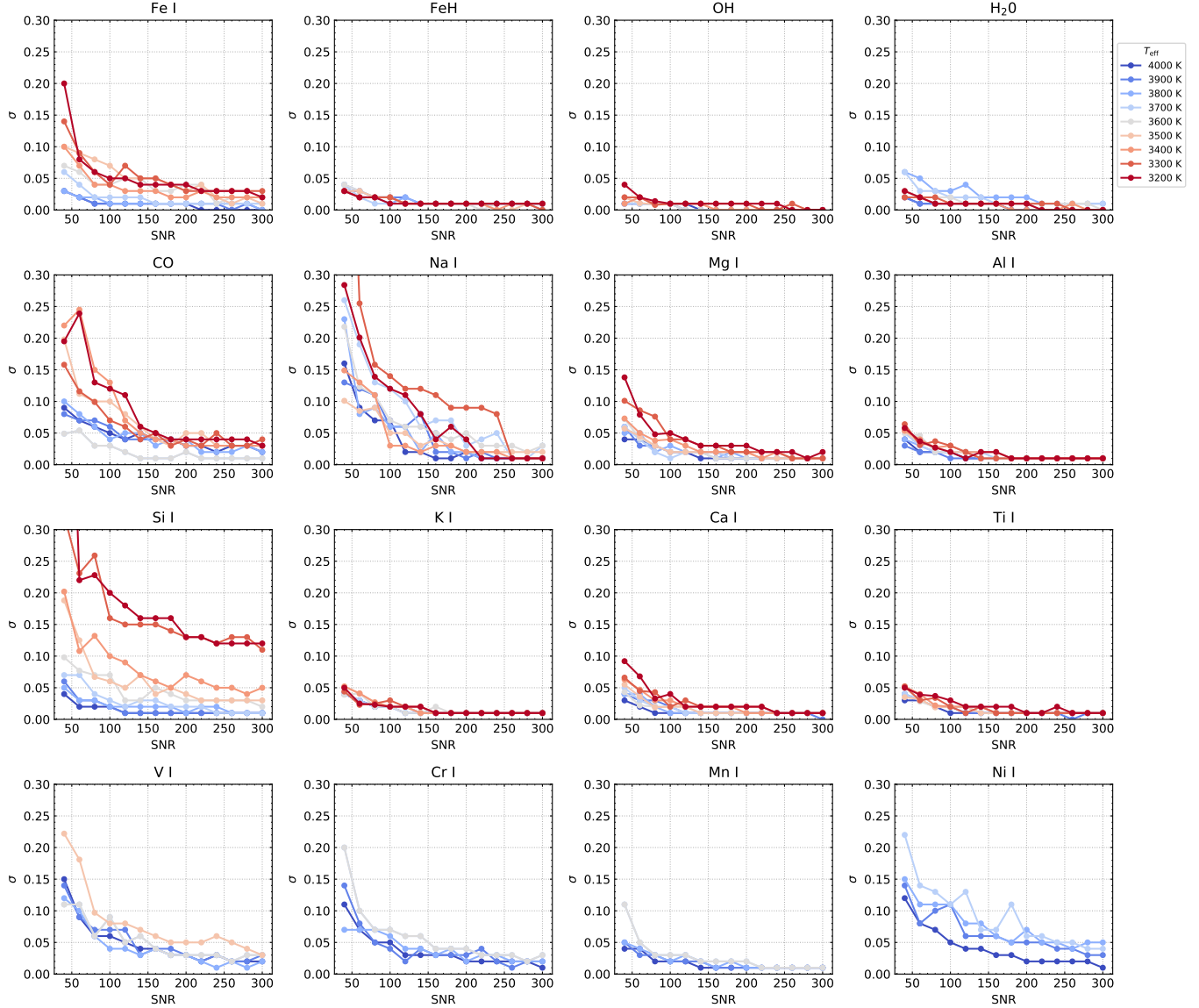


**Figure 3.** Signal-to-noise (SNR) versus uncertainties due to changes in the signal-to-noise ratio ( $\sigma_{\text{SNR}}$ ).

remains close to 0.05 dex. For Si, when  $T_{\text{eff}}$  is 3300K,  $\sigma_{\text{SNR}}$  consistently exceeds 0.10 dex regardless of the adopted SNR.

### A.3. Uncertainties due to changes in the pseudo-continuum definition

The complexity of M dwarf spectra poses challenges in defining the pseudo-continuum, which is expected to be transition-free. Consequently, uncertainties in pseudo-continuum definition can lead to shifts in the normalized spectral synthesis flux, influencing the measurement of abundances and introducing associated uncertainties. This section lists uncertainties due to pseudo-continuum shifts ( $\sigma_{\text{PC}}$ ). To evaluate uncertainties associated with variations in the pseudo-continuum, we utilize the spectral synthesis grid (discussed in Section A.1) as our “observed spectra” and calculate individual line abundances for all studied elements. We introduce shifts of -2%, -1%, +1%, and +2% in the normalized flux of the “observed spectra” and then compute their abundances. We consider a  $\pm 2\%$  deviation in the normalized flux spectra as lower and upper limits of shifts. Changes beyond this range make determining abundances challenging (or impossible) for most species. We define our  $\sigma_{\text{PC}}$  as the difference between the individual abundance derived with and without the shift in the normalized flux spectra.

Table 6 summarizes uncertainties in pseudo-continuum displacement at temperatures ranging from 4000 to 3200K for all studied species. Each row in the table corresponds to a specific element, while the columns represent percentage variations in pseudo-continuum displacement relative to the reference condition, including  $\pm 2\%$  and  $\pm 1\%$ . The values in each table cell indicate the abundance change for the respective element under these conditions.

The uncertainties here are usually more significant for weaker lines. For Na, V, Cr, and Ni, for example, the uncertainty can be higher than 0.20 dex, assuming  $\pm 2\%$  shifts. For most species, the  $\sigma_{PC}$  is smaller than 0.10 for shifts of  $\pm 1\%$  in the pseudo-continuum definition. These values are valuable for interpreting spectroscopic analyses and quantifying uncertainties, facilitating a more precise understanding of how pseudo-continuum displacement variations impact the abundance of different elements.



**Table 4** (*continued*)

Element	$T_{\text{eff}}$			$\log g$			Fe/H			$\xi$			
	+100	-50	-100	+0.20	+0.10	-0.10	+0.20	+0.10	-0.10	+0.50	+0.25	-0.25	-0.50
	(K)	(K)	(K)	(dex)	(dex)	(dex)	(dex)	(dex)	(dex)	(km.s <sup>-1</sup> )	(km.s <sup>-1</sup> )	(km.s <sup>-1</sup> )	(km.s <sup>-1</sup> )
Ni Assuming $T_{\text{eff}} = 3700$ K													
Fe (FeI)	-0.11	-0.06	0.09	0.20	0.19	0.10	-0.08	-0.15	0.03	0.01	0.06	0.10	0.00
Fe (FeH)	0.05	0.02	-0.02	-0.04	0.03	0.01	-0.02	-0.04	0.11	0.05	-0.06	-0.12	-0.05
C	0.02	0.01	-0.01	0.00	0.04	0.02	-0.03	-0.05	0.11	0.01	-0.07	-0.15	0.00
O (H <sub>2</sub> O)	0.09	0.04	-0.03	-0.06	-0.01	-0.01	0.00	0.00	0.30	0.24	-0.11	-0.21	-0.01
O (OH)	0.00	0.00	0.00	0.00	0.02	0.01	-0.01	-0.04	0.06	0.01	-0.08	-0.17	-0.02
Na	0.01	0.00	-0.01	-0.02	0.12	0.03	-0.02	-0.04	0.24	0.08	0.07	0.16	0.00
Mg	-0.24	-0.13	0.12	0.22	0.15	0.08	-0.08	-0.17	-0.06	-0.03	0.03	0.04	0.00
Al	-0.11	-0.05	0.04	0.09	0.06	0.03	-0.04	-0.09	-0.03	-0.01	0.00	-0.01	-0.01
Si	-0.27	-0.14	0.13	0.27	0.23	0.13	-0.12	-0.23	-0.08	-0.04	0.07	0.09	0.00
K	0.05	0.03	-0.01	-0.01	0.03	0.02	-0.01	-0.02	0.00	0.00	0.02	0.03	0.00
Ca	-0.04	-0.01	0.02	0.04	0.10	0.05	-0.06	-0.12	-0.07	-0.03	0.04	0.08	0.00
Ti	-0.02	-0.01	0.01	0.02	0.07	0.04	-0.04	-0.08	0.04	0.01	-0.01	-0.03	-0.02
V	0.09	0.05	-0.02	-0.03	0.12	0.07	-0.05	-0.09	0.10	0.04	0.02	0.01	0.00
Cr	-0.12	-0.06	0.09	0.17	0.17	0.09	-0.07	-0.12	0.03	0.00	0.06	0.07	0.00
Mn	-0.08	-0.05	0.06	0.14	0.16	0.08	-0.07	-0.13	0.04	0.01	0.05	0.08	0.00
Ni	0.35	0.08	0.21	0.23	0.31	0.23	-0.06	0.01	0.23	-0.05	0.21	0.26	0.00
Assuming $T_{\text{eff}} = 3600$ K													
Fe (FeI)	-0.12	-0.06	0.08	0.17	0.18	0.08	-0.06	-0.13	0.05	0.02	0.06	0.10	0.00
Fe (FeH)	0.06	0.03	-0.02	-0.03	0.03	0.01	-0.01	-0.02	0.13	0.07	-0.07	-0.13	-0.05
C	0.02	0.01	-0.01	-0.02	0.03	0.02	-0.02	-0.05	0.08	-0.01	-0.08	-0.16	0.00
O (H <sub>2</sub> O)	0.08	0.04	-0.03	-0.06	-0.01	0.00	0.00	0.00	0.02	0.10	-0.10	-0.32	0.00
O (OH)	-0.01	0.00	0.00	0.00	0.01	0.01	-0.02	-0.05	0.06	0.00	-0.09	-0.18	-0.02
Na	-0.02	-0.01	-0.01	-0.04	0.08	0.02	-0.01	-0.02	0.20	0.09	-0.01	0.00	0.00
Mg	-0.21	-0.11	0.11	0.20	0.13	0.07	-0.08	-0.16	-0.04	-0.03	0.02	0.02	-0.01
Al	-0.13	-0.05	0.06	0.10	0.07	0.03	-0.04	-0.08	-0.01	0.00	0.00	-0.01	0.00
Si	-0.27	-0.13	0.16	0.27	0.21	0.11	-0.11	-0.20	-0.02	-0.01	0.04	0.05	-0.02
K	0.06	0.03	-0.03	-0.04	0.00	0.00	-0.01	-0.02	0.00	0.00	0.01	0.01	-0.01
Ca	-0.05	-0.02	0.02	0.04	0.10	0.05	-0.05	-0.11	-0.06	-0.03	0.04	0.08	0.00
Ti	-0.03	-0.01	0.02	0.04	0.04	0.02	-0.02	-0.04	0.07	0.03	-0.03	-0.07	0.00
V	0.10	0.05	-0.02	-0.03	0.13	0.08	-0.05	-0.09	0.11	0.06	0.04	0.02	0.00
Mn	0.11	0.03	0.01	0.02	0.14	0.06	-0.05	-0.09	0.14	0.07	0.07	0.14	0.00
Assuming $T_{\text{eff}} = 3500$ K													
Fe (FeI)	-0.18	-0.09	0.09	0.19	0.09	0.05	-0.07	-0.12	0.00	0.00	-0.01	0.00	0.00
Fe (FeH)	0.07	0.03	-0.03	-0.06	0.02	0.01	-0.01	-0.01	0.15	0.07	-0.07	-0.15	-0.05

**Table 4** *continued*



Table 4 (*continued*)

Element	$T_{\text{eff}}$		Log $g$		Fe/H		$\xi$				
	+100	+50	-100	+0.10	-0.10	+0.20	-0.20	+0.50	+0.25	-0.25	-0.50
	(K)	(K)	(dex)	(dex)	(dex)	(dex)	(dex)	(dex)	(km.s $^{-1}$ )	(km.s $^{-1}$ )	(km.s $^{-1}$ )
Ca	-0.12	-0.06	0.05	0.09	0.14	0.07	-0.08	-0.15	-0.03	0.02	0.06
Ti	-0.04	-0.01	0.02	0.04	0.03	0.01	-0.01	-0.03	0.08	0.04	-0.07
Assuming $T_{\text{eff}} = 3200$ K											
Fe (FeI)	0.09	0.05	-0.03	-0.06	0.00	0.01	0.02	0.18	0.09	-0.08	-0.17
Fe (FeH)	0.02	0.01	0.00	0.01	0.01	0.01	0.00	0.08	0.01	-0.09	-0.18
C	0.05	0.03	-0.03	-0.05	0.00	0.00	0.00	0.13	0.07	-0.10	-0.19
O (H <sub>2</sub> O)	0.00	0.00	-0.01	0.00	0.00	-0.01	-0.07	0.07	0.01	-0.10	-0.18
O (OH)	0.03	0.01	-0.02	-0.03	0.04	0.01	-0.02	-0.04	0.54	0.05	-0.04
Na	-0.14	-0.07	0.08	0.18	0.16	0.07	-0.07	-0.13	0.03	0.01	0.00
Mg	-0.15	-0.08	0.07	0.13	0.07	0.04	-0.06	-0.11	0.00	-0.03	-0.07
Al	0.75	0.00	0.52	0.75	-0.06	-0.03	0.04	0.53	0.10	0.04	-0.15
Si	0.13	0.06	-0.07	-0.12	-0.08	-0.04	0.03	0.05	0.03	0.02	-0.05
K	-0.16	-0.08	0.06	0.11	0.15	0.07	-0.10	-0.17	-0.06	-0.03	0.01
Ca	-0.02	-0.01	0.02	0.04	0.01	0.01	0.00	-0.02	0.08	0.04	-0.08
Ti									-0.01	0.00	0.02

**Table 5.** Uncertainties due to signal-to-noise ratio (SNR) changes.

SNR	4000K	3900K	3800K	3700K	3600K	3500K	3400K	3300K	3200K
A(Fe) from Fe I lines									
40	0.03	0.03	0.03	0.06	0.07	0.10	0.10	0.14	0.20
60	0.02	0.02	0.02	0.04	0.06	0.09	0.07	0.09	0.08
80	0.01	0.01	0.02	0.02	0.04	0.08	0.04	0.06	0.06
100	0.01	0.01	0.01	0.02	0.04	0.07	0.04	0.04	0.05
120	0.01	0.01	0.01	0.02	0.05	0.05	0.03	0.07	0.05
140	0.01	0.01	0.01	0.02	0.05	0.05	0.03	0.05	0.04
160	0.01	0.01	0.01	0.01	0.03	0.05	0.03	0.05	0.04
180	0.01	0.01	0.01	0.01	0.03	0.04	0.02	0.04	0.04
200	0.01	0.01	0.01	0.01	0.04	0.03	0.02	0.03	0.04
220	0.00	0.01	0.01	0.01	0.04	0.04	0.03	0.03	0.03
240	0.00	0.01	0.01	0.01	0.01	0.02	0.02	0.03	0.03
260	0.00	0.00	0.01	0.01	0.02	0.01	0.02	0.03	0.03
280	0.00	0.01	0.01	0.01	0.02	0.02	0.02	0.03	0.03
300+	0.00	0.00	0.00	0.01	0.02	0.01	0.02	0.03	0.02
A(Fe) from FeH lines									
40	0.03	0.03	0.04	0.04	0.04	0.03	0.03	0.03	0.03
60	0.03	0.02	0.03	0.02	0.03	0.03	0.02	0.02	0.02
80	0.02	0.02	0.02	0.01	0.02	0.02	0.02	0.02	0.02
100	0.02	0.02	0.01	0.01	0.02	0.02	0.02	0.02	0.01
120	0.01	0.02	0.02	0.01	0.01	0.01	0.01	0.01	0.01
140	0.01	0.01	0.01	0.01	0.01	0.01	0.01	0.01	0.01
160	0.01	0.01	0.01	0.01	0.01	0.01	0.01	0.01	0.01
180	0.01	0.01	0.01	0.01	0.01	0.01	0.01	0.01	0.01
200	0.01	0.01	0.01	0.01	0.01	0.01	0.01	0.01	0.01
220	0.01	0.01	0.01	0.01	0.00	0.01	0.01	0.01	0.01
240	0.01	0.01	0.01	0.01	0.01	0.00	0.00	0.01	0.01
260	0.01	0.01	0.01	0.01	0.01	0.00	0.01	0.01	0.01
280	0.01	0.01	0.01	0.01	0.01	0.01	0.01	0.01	0.01
300+	0.01	0.01	0.00	0.01	0.01	0.00	0.01	0.00	0.01
A(O) from OH lines									
40	0.01	0.01	0.01	0.01	0.02	0.02	0.01	0.02	0.04
60	0.01	0.01	0.01	0.01	0.01	0.01	0.02	0.02	0.02
80	0.01	0.01	0.01	0.01	0.01	0.01	0.01	0.01	0.01
100	0.01	0.01	0.01	0.01	0.01	0.01	0.01	0.01	0.01
120	0.01	0.00	0.00	0.00	0.00	0.01	0.01	0.01	0.01
140	0.00	0.00	0.00	0.00	0.00	0.01	0.01	0.01	0.01
160	0.00	0.00	0.00	0.00	0.00	0.00	0.00	0.01	0.01
180	0.00	0.00	0.00	0.00	0.00	0.00	0.00	0.01	0.01
200	0.00	0.00	0.00	0.00	0.00	0.00	0.00	0.01	0.01
220	0.00	0.00	0.00	0.00	0.00	0.00	0.00	0.00	0.01
240	0.00	0.00	0.00	0.00	0.00	0.00	0.00	0.00	0.01
260	0.00	0.00	0.00	0.00	0.00	0.00	0.00	0.01	0.00
280	0.00	0.00	0.00	0.00	0.00	0.00	0.00	0.00	0.00
300+	0.00	0.00	0.00	0.00	0.00	0.00	0.00	0.00	0.00
A(O) from H <sub>2</sub> O lines									
40	0.02	0.02	0.06	0.06	0.03	0.03	0.02	0.02	0.03
60	0.01	0.01	0.05	0.03	0.02	0.02	0.02	0.02	0.02
80	0.01	0.01	0.03	0.03	0.02	0.01	0.01	0.02	0.01
100	0.01	0.01	0.03	0.02	0.02	0.01	0.01	0.01	0.01
120	0.01	0.01	0.04	0.02	0.01	0.01	0.01	0.01	0.01

**Table 5** *continued*

**Table 5** (*continued*)

SNR	4000K	3900K	3800K	3700K	3600K	3500K	3400K	3300K	3200K
140	0.01	0.01	0.02	0.02	0.01	0.01	0.01	0.01	0.01
160	0.01	0.01	0.02	0.01	0.01	0.01	0.01	0.01	0.01
180	0.00	0.00	0.02	0.01	0.01	0.01	0.00	0.01	0.01
200	0.00	0.00	0.02	0.01	0.01	0.01	0.00	0.01	0.01
220	0.00	0.00	0.01	0.01	0.01	0.00	0.00	0.01	0.00
240	0.00	0.00	0.01	0.01	0.01	0.00	0.00	0.01	0.00
260	0.00	0.00	0.01	0.01	0.01	0.00	0.01	0.00	0.00
280	0.00	0.00	0.01	0.01	0.01	0.00	0.00	0.00	0.00
300+	0.00	0.00	0.01	0.01	0.00	0.00	0.00	0.00	0.00
A(C) from CO lines									
40	0.09	0.08	0.10	0.05	0.05	0.20	0.22	0.16	0.20
60	0.07	0.07	0.08	0.05	0.05	0.11	0.24	0.12	0.24
80	0.06	0.07	0.06	0.03	0.03	0.10	0.15	0.10	0.13
100	0.05	0.06	0.04	0.03	0.03	0.10	0.13	0.07	0.12
120	0.04	0.04	0.05	0.02	0.02	0.08	0.07	0.06	0.11
140	0.05	0.04	0.05	0.01	0.01	0.06	0.05	0.04	0.06
160	0.04	0.04	0.03	0.01	0.01	0.04	0.04	0.05	0.05
180	0.04	0.04	0.04	0.01	0.01	0.03	0.04	0.03	0.04
200	0.03	0.03	0.04	0.02	0.02	0.05	0.03	0.04	0.04
220	0.03	0.03	0.02	0.01	0.01	0.05	0.03	0.03	0.04
240	0.02	0.03	0.02	0.01	0.01	0.03	0.03	0.05	0.04
260	0.03	0.03	0.02	0.01	0.01	0.03	0.03	0.03	0.04
280	0.03	0.03	0.03	0.01	0.01	0.03	0.03	0.03	0.04
300+	0.02	0.03	0.02	0.01	0.01	0.03	0.03	0.04	0.03
A(Na) from Na I lines									
40	0.16	0.13	0.23	0.26	0.22	0.10	0.15	0.84	0.28
60	0.09	0.12	0.08	0.19	0.12	0.08	0.13	0.26	0.20
80	0.07	0.11	0.09	0.13	0.11	0.09	0.11	0.16	0.14
100	0.07	0.06	0.06	0.12	0.07	0.05	0.03	0.14	0.12
120	0.02	0.06	0.06	0.10	0.06	0.05	0.03	0.12	0.11
140	0.02	0.08	0.02	0.06	0.06	0.03	0.02	0.12	0.08
160	0.01	0.02	0.05	0.07	0.05	0.04	0.03	0.11	0.04
180	0.01	0.02	0.02	0.07	0.04	0.03	0.03	0.09	0.06
200	0.02	0.01	0.02	0.03	0.05	0.02	0.02	0.09	0.04
220	0.01	0.02	0.01	0.04	0.03	0.02	0.02	0.09	0.01
240	0.01	0.01	0.01	0.05	0.03	0.02	0.02	0.08	0.01
260	0.01	0.01	0.01	0.01	0.03	0.02	0.01	0.01	0.01
280	0.01	0.01	0.01	0.01	0.02	0.02	0.01	0.01	0.01
300+	0.01	0.01	0.01	0.03	0.03	0.02	0.01	0.01	0.01
A(Mg) from Mg I lines									
40	0.04	0.06	0.05	0.06	0.07	0.06	0.07	0.10	0.14
60	0.04	0.03	0.05	0.04	0.04	0.04	0.05	0.09	0.08
80	0.03	0.03	0.02	0.02	0.03	0.03	0.04	0.08	0.05
100	0.02	0.02	0.03	0.01	0.02	0.02	0.04	0.04	0.05
120	0.02	0.02	0.02	0.02	0.02	0.02	0.03	0.04	0.04
140	0.01	0.02	0.02	0.02	0.02	0.02	0.02	0.03	0.03
160	0.01	0.02	0.01	0.02	0.01	0.02	0.02	0.03	0.03
180	0.01	0.01	0.02	0.01	0.01	0.02	0.02	0.02	0.03
200	0.01	0.01	0.01	0.01	0.01	0.02	0.02	0.02	0.03
220	0.01	0.01	0.01	0.01	0.01	0.01	0.01	0.02	0.02
240	0.01	0.01	0.01	0.01	0.01	0.01	0.02	0.02	0.02
260	0.01	0.01	0.01	0.01	0.01	0.01	0.01	0.01	0.02
280	0.01	0.01	0.01	0.01	0.01	0.01	0.01	0.01	0.01
300+	0.01	0.01	0.01	0.01	0.01	0.01	0.01	0.01	0.02

**Table 5** *continued*

**Table 5** (*continued*)

SNR	4000K	3900K	3800K	3700K	3600K	3500K	3400K	3300K	3200K
A(Al) from Al I lines									
40	0.04	0.03	0.04	0.05	0.05	0.05	0.05	0.06	0.06
60	0.02	0.02	0.03	0.03	0.05	0.03	0.04	0.03	0.04
80	0.02	0.02	0.02	0.02	0.02	0.03	0.03	0.04	0.03
100	0.02	0.01	0.02	0.02	0.02	0.02	0.03	0.03	0.02
120	0.01	0.01	0.02	0.02	0.02	0.02	0.02	0.02	0.01
140	0.01	0.01	0.01	0.02	0.01	0.01	0.02	0.01	0.02
160	0.01	0.01	0.01	0.01	0.01	0.01	0.02	0.01	0.02
180	0.01	0.01	0.01	0.01	0.01	0.01	0.01	0.01	0.01
200	0.01	0.01	0.01	0.01	0.01	0.01	0.01	0.01	0.01
220	0.01	0.01	0.01	0.01	0.01	0.01	0.01	0.01	0.01
240	0.01	0.01	0.01	0.01	0.01	0.01	0.01	0.01	0.01
260	0.01	0.01	0.01	0.01	0.01	0.01	0.01	0.01	0.01
280	0.01	0.01	0.01	0.01	0.01	0.01	0.01	0.01	0.01
300+	0.01	0.01	0.01	0.01	0.01	0.01	0.01	0.01	0.01
A(Si) from Si I lines									
40	0.04	0.06	0.05	0.07	0.10	0.19	0.20	0.32	0.91
60	0.02	0.03	0.03	0.07	0.08	0.12	0.11	0.23	0.22
80	0.02	0.03	0.03	0.04	0.07	0.07	0.13	0.26	0.23
100	0.02	0.02	0.02	0.03	0.07	0.06	0.10	0.16	0.20
120	0.01	0.01	0.02	0.02	0.03	0.05	0.09	0.15	0.18
140	0.01	0.01	0.02	0.03	0.03	0.07	0.07	0.15	0.16
160	0.01	0.01	0.02	0.03	0.05	0.04	0.06	0.15	0.16
180	0.01	0.01	0.02	0.02	0.04	0.05	0.05	0.14	0.16
200	0.01	0.01	0.01	0.02	0.03	0.04	0.07	0.13	0.13
220	0.01	0.01	0.02	0.02	0.03	0.03	0.06	0.13	0.13
240	0.01	0.01	0.02	0.01	0.03	0.03	0.05	0.12	0.12
260	0.01	0.01	0.01	0.01	0.03	0.03	0.05	0.13	0.12
280	0.01	0.01	0.01	0.01	0.03	0.03	0.04	0.13	0.12
300+	0.01	0.01	0.01	0.01	0.02	0.03	0.05	0.11	0.12
A(K) from K I lines									
40	0.04	0.04	0.04	0.04	0.04	0.05	0.05	0.04	0.05
60	0.03	0.03	0.03	0.03	0.04	0.04	0.04	0.02	0.02
80	0.02	0.02	0.02	0.02	0.02	0.03	0.03	0.02	0.02
100	0.02	0.02	0.02	0.02	0.02	0.02	0.02	0.03	0.02
120	0.02	0.01	0.01	0.02	0.01	0.02	0.02	0.02	0.02
140	0.01	0.01	0.01	0.01	0.01	0.01	0.01	0.02	0.02
160	0.01	0.01	0.01	0.01	0.02	0.01	0.01	0.01	0.01
180	0.01	0.01	0.01	0.01	0.01	0.01	0.01	0.01	0.01
200	0.01	0.01	0.01	0.01	0.01	0.01	0.01	0.01	0.01
220	0.01	0.01	0.01	0.01	0.01	0.01	0.01	0.01	0.01
240	0.01	0.01	0.01	0.01	0.01	0.01	0.01	0.01	0.01
260	0.01	0.01	0.01	0.01	0.01	0.01	0.01	0.01	0.01
280	0.01	0.01	0.01	0.01	0.01	0.01	0.01	0.01	0.01
300+	0.01	0.01	0.01	0.01	0.01	0.01	0.01	0.01	0.01
A(Ca) from Ca I lines									
40	0.03	0.04	0.04	0.05	0.04	0.05	0.06	0.07	0.09
60	0.02	0.03	0.04	0.03	0.02	0.04	0.05	0.04	0.07
80	0.01	0.03	0.02	0.02	0.02	0.02	0.03	0.04	0.03
100	0.01	0.02	0.01	0.02	0.02	0.02	0.03	0.02	0.04
120	0.01	0.01	0.01	0.01	0.02	0.02	0.02	0.03	0.02
140	0.01	0.01	0.01	0.01	0.01	0.01	0.02	0.02	0.02
160	0.01	0.01	0.01	0.01	0.01	0.01	0.02	0.02	0.02
180	0.01	0.01	0.01	0.01	0.01	0.01	0.02	0.02	0.02

**Table 5** *continued*

**Table 5** (*continued*)

SNR	4000K	3900K	3800K	3700K	3600K	3500K	3400K	3300K	3200K
200	0.01	0.01	0.01	0.01	0.01	0.01	0.01	0.02	0.02
220	0.01	0.01	0.01	0.01	0.01	0.01	0.01	0.02	0.02
240	0.01	0.01	0.01	0.01	0.01	0.01	0.01	0.01	0.01
260	0.01	0.01	0.01	0.01	0.01	0.01	0.01	0.01	0.01
280	0.01	0.01	0.01	0.01	0.01	0.01	0.01	0.01	0.01
300+	0.01	0.00	0.01	0.01	0.01	0.01	0.01	0.01	0.01
A(Ti) from Ti I lines									
40	0.03	0.04	0.04	0.04	0.05	0.03	0.05	0.05	0.05
60	0.03	0.03	0.03	0.03	0.03	0.03	0.04	0.03	0.04
80	0.02	0.02	0.02	0.02	0.02	0.02	0.02	0.03	0.04
100	0.01	0.02	0.02	0.02	0.02	0.02	0.02	0.02	0.03
120	0.01	0.01	0.02	0.02	0.02	0.02	0.02	0.01	0.02
140	0.01	0.01	0.01	0.02	0.01	0.01	0.02	0.02	0.02
160	0.01	0.01	0.01	0.01	0.01	0.01	0.01	0.01	0.02
180	0.01	0.01	0.01	0.01	0.01	0.01	0.01	0.01	0.02
200	0.01	0.01	0.01	0.01	0.01	0.01	0.01	0.01	0.01
220	0.01	0.01	0.01	0.01	0.01	0.01	0.01	0.01	0.01
240	0.01	0.01	0.01	0.01	0.01	0.01	0.01	0.01	0.02
260	0.01	0.00	0.01	0.01	0.01	0.01	0.01	0.01	0.01
280	0.01	0.01	0.01	0.01	0.01	0.01	0.01	0.01	0.01
300+	0.01	0.01	0.01	0.01	0.01	0.01	0.01	0.01	0.01
A(V) from V I lines									
40	0.15	0.14	0.12	0.11	0.11	0.22			
60	0.09	0.09	0.10	0.11	0.11	0.18			
80	0.06	0.07	0.06	0.06	0.06	0.10			
100	0.06	0.07	0.04	0.09	0.09	0.08			
120	0.05	0.07	0.04	0.05	0.05	0.08			
140	0.04	0.03	0.03	0.06	0.06	0.07			
160	0.04	0.04	0.04	0.04	0.04	0.06			
180	0.03	0.04	0.03	0.03	0.03	0.05			
200	0.03	0.03	0.03	0.03	0.03	0.05			
220	0.02	0.02	0.02	0.03	0.03	0.05			
240	0.03	0.03	0.01	0.03	0.03	0.06			
260	0.02	0.02	0.02	0.02	0.02	0.05			
280	0.02	0.02	0.01	0.03	0.03	0.04			
300+	0.02	0.03	0.02	0.03	0.03	0.03			
A(Cr) from Cr I lines									
40	0.11	0.14	0.07	0.20	0.20				
60	0.07	0.08	0.07	0.10	0.10				
80	0.05	0.05	0.07	0.07	0.07				
100	0.05	0.04	0.06	0.07	0.07				
120	0.03	0.02	0.04	0.06	0.06				
140	0.03	0.04	0.04	0.06	0.06				
160	0.03	0.03	0.03	0.04	0.04				
180	0.03	0.03	0.04	0.04	0.04				
200	0.02	0.03	0.02	0.04	0.04				
220	0.02	0.04	0.03	0.03	0.03				
240	0.02	0.02	0.03	0.03	0.03				
260	0.02	0.01	0.02	0.03	0.03				
280	0.02	0.02	0.02	0.02	0.02				
300+	0.01	0.02	0.02	0.03	0.03				
A(Mn) from Mn I lines									
40	0.04	0.05	0.05	0.11	0.11				
60	0.04	0.03	0.04	0.05	0.05				

**Table 5** *continued*

**Table 5** (*continued*)

SNR	4000K	3900K	3800K	3700K	3600K	3500K	3400K	3300K	3200K
80	0.02	0.03	0.03	0.03	0.03				
100	0.02	0.02	0.02	0.03	0.03				
120	0.02	0.02	0.03	0.03	0.03				
140	0.01	0.02	0.02	0.02	0.02				
160	0.01	0.01	0.01	0.02	0.02				
180	0.01	0.01	0.02	0.02	0.02				
200	0.01	0.01	0.01	0.02	0.02				
220	0.01	0.01	0.01	0.01	0.01				
240	0.01	0.01	0.01	0.01	0.01				
260	0.01	0.01	0.01	0.01	0.01				
280	0.01	0.01	0.01	0.01	0.01				
300+	0.01	0.01	0.01	0.01	0.01				
A(Ni) from Ni I lines									
40	0.12	0.14	0.15	0.22					
60	0.08	0.08	0.11	0.14					
80	0.07	0.10	0.11	0.13					
100	0.05	0.11	0.11	0.11					
120	0.04	0.06	0.08	0.13					
140	0.04	0.06	0.08	0.07					
160	0.03	0.06	0.06	0.07					
180	0.03	0.05	0.05	0.11					
200	0.02	0.05	0.07	0.06					
220	0.02	0.05	0.05	0.06					
240	0.02	0.04	0.05	0.05					
260	0.02	0.04	0.04	0.05					
280	0.02	0.03	0.05	0.04					
300+	0.01	0.03	0.05	0.04					

300+ indicates that SNR higher than 300 can also adopt the values.

**Table 6.** Uncertainties due to pseudo-continuum displacements.

Pseudocontinuum displacement	4000K	3900K	3800K	3700K	3600K	3500K	3400K	3300K	3200K
A(Fe) from Fe I lines									
-2%	-0.147	-0.181	-0.209	-0.335	-0.287	-0.334	-0.227	-0.316	-0.316
-1%	-0.072	-0.088	-0.098	-0.160	-0.135	-0.163	-0.113	-0.155	-0.155
+1%	0.072	0.084	0.088	0.119	0.119	0.136	0.111	0.085	0.085
+2%	0.137	0.157	0.168	0.209	0.206	0.226	0.211	0.156	0.156
A(Fe) from FeH lines									
-2%	-0.224	-0.226	-0.227	-0.252	-0.226	-0.190	-0.196	-0.202	-0.177
-1%	-0.124	-0.119	-0.118	-0.132	-0.115	-0.112	-0.107	-0.098	-0.099
+1%	0.100	0.099	0.098	0.101	0.079	0.083	0.083	0.099	0.078
+2%	0.178	0.177	0.176	0.180	0.137	0.144	0.143	0.175	0.158
A(O) from OH lines									
-2%	-0.033	-0.031	-0.027	-0.033	-0.040	-0.057	-0.056	-0.055	-0.065
-1%	-0.015	-0.015	-0.012	-0.016	-0.023	-0.030	-0.024	-0.024	-0.029
+1%	0.027	0.026	0.028	0.037	0.036	0.022	0.017	0.030	0.025
+2%	0.060	0.061	0.072	0.081	0.075	0.062	0.059	0.068	0.056
A(O) from H <sub>2</sub> O lines									

**Table 6** *continued*



**Table 6** (*continued*)

Pseudocontinuum displacement	4000K	3900K	3800K	3700K	3600K	3500K	3400K	3300K	3200K
A(Mn) from Mn I lines									
-2%	-0.146	-0.172	-0.212	-0.306	-0.427	-0.541			
-1%	-0.071	-0.083	-0.101	-0.143	-0.190	-0.265			
+1%	0.064	0.072	0.085	0.104	0.122	0.140			
+2%	0.121	0.137	0.156	0.180	0.208	0.245			
A(Ni) from Ni I lines									
-2%	-0.500	-0.456	-0.490	-0.574					
-1%	-0.345	-0.272	-0.304	-0.342					
+1%	0.223	0.277	0.264	0.248					
+2%	0.321	0.398	0.411	0.327					

## REFERENCES

- Abdurro'uf, Accetta, K., Aerts, C., et al. 2022, ApJS, 259, 35. doi:10.3847/1538-4365/ac4414
- Adams, E. R., Seager, S., & Elkins-Tanton, L. 2008, ApJ, 673, 1160. doi:10.1086/524925
- Adibekyan, V. Z., Sousa, S. G., Santos, N. C., et al. 2012, A&A, 545, A32. doi:10.1051/0004-6361/201219401
- Ahumada, R., Allende Prieto, C., Almeida, A., et al. 2020, ApJS, 249, 3. doi:10.3847/1538-4365/ab929e
- Allard, F., Hauschildt, P. H., & Schwenke, D. 2000, ApJ, 540, 1005. doi:10.1086/309366
- Allart, R., Bourrier, V., Lovis, C., et al. 2019, A&A, 623, A58. doi:10.1051/0004-6361/201834917
- Alonso-Floriano, F. J., Snellen, I. A. G., Czesla, S., et al. 2019, A&A, 629, A110. doi:10.1051/0004-6361/201935979
- Alvarez, R. & Plez, B. 1998, A&A, 330, 1109. doi:10.48550/arXiv.astro-ph/9710157
- Antoniadis-Karnavas, A., Sousa, S. G., Delgado-Mena, E., et al. 2020, A&A, 636, A9. doi:10.1051/0004-6361/201937194
- Artigau, É., Kouach, D., Donati, J.-F., et al. 2014, Proc. SPIE, 9147, 914715. doi:10.1117/12.2055663
- Asplund, M., Amarsi, A. M., & Grevesse, N. 2021, A&A, 653, A141. doi:10.1051/0004-6361/202140445
- Awiphan, S., Kerins, E., Pichadee, S., et al. 2016, MNRAS, 463, 2574. doi:10.1093/mnras/stw2148
- Bailer-Jones, C. A. L., Rybizki, J., Fouesneau, M., et al. 2021, AJ, 161, 147. doi:10.3847/1538-3881/abd806
- Benneke, B., Knutson, H. A., Lothringer, J., et al. 2019, Nature Astronomy, 3, 813. doi:10.1038/s41550-019-0800-5
- Benneke, B., Mikal-Evans, T., Acuna, L., et al. 2023, JWST Proposal. Cycle 2, 4098
- Birky, J., Hogg, D. W., Mann, A. W., et al. 2020, ApJ, 892, 31. doi:10.3847/1538-4357/ab7004
- Bluhm, P., Pallé, E., Molaverdikhani, K., et al. 2021, A&A, 650, A78. doi:10.1051/0004-6361/202140688
- Biddle, L. I., Pearson, K. A., Crossfield, I. J. M., et al. 2014, MNRAS, 443, 1810. doi:10.1093/mnras/stu1199
- Boeche, C. & Grebel, E. K. 2016, A&A, 587, A2. doi:10.1051/0004-6361/201526758
- Bond, J. C., O'Brien, D. P., & Lauretta, D. S. 2010, ApJ, 715, 1050. doi:10.1088/0004-637X/715/2/1050
- Bonfils, X., Gillon, M., Udry, S., et al. 2012, A&A, 546, A27. doi:10.1051/0004-6361/201219623
- Bourrier, V., Lecavelier des Etangs, A., Ehrenreich, D., et al. 2018, A&A, 620, A147. doi:10.1051/0004-6361/201833675
- Bourrier, V., Lovis, C., Beust, H., et al. 2018, Nature, 553, 477. doi:10.1038/nature24677
- Butler, R. P., Vogt, S. S., Marcy, G. W., et al. 2004, ApJ, 617, 580. doi:10.1086/425173
- Chabrier, G., Gallardo, J., & Baraffe, I. 2007, A&A, 472, L17. doi:10.1051/0004-6361:200777702
- Charbonneau, D. & Deming, D. 2007, arXiv:0706.1047. doi:10.48550/arXiv.0706.1047
- Cincunegui, C., Díaz, R. F., & Mauas, P. J. D. 2007, A&A, 469, 309. doi:10.1051/0004-6361:20066503
- Cristofari, P. I., Donati, J.-F., Folsom, C. P., et al. 2023, MNRAS, 522, 1342. doi:10.1093/mnras/stad865
- Crossfield, I. J. M. 2023, ApJL, 952, L18. doi:10.3847/2041-8213/ace35f
- Crossfield, I. J. M., Barman, T., Hansen, B. M. S., et al. 2013, A&A, 559, A33. doi:10.1051/0004-6361/201322278

- Cutri, R. M., Nelson, B. O., Francis, P. J., et al. 2002, IAU Colloq. 184: AGN Surveys, 284, 127
- Delgado Mena, E., Adibekyan, V., Santos, N. C., et al. 2021, A&A, 655, A99. doi:10.1051/0004-6361/202141588
- Delgado Mena, E., Israelián, G., González Hernández, J. I., et al. 2010, ApJ, 725, 2349. doi:10.1088/0004-637X/725/2/2349
- Ding, M.-Y., Shi, J.-R., Wu, Y., et al. 2022, ApJS, 260, 45. doi:10.3847/1538-4365/ac6754
- Donati, J.-F., Kouach, D., Moutou, C., et al. 2020, MNRAS, 498, 5684. doi:10.1093/mnras/staa2569
- Dorn, C., Hinkel, N. R., & Venturini, J. 2017, A&A, 597, A38. doi:10.1051/0004-6361/201628749
- Dorn, C., Khan, A., Heng, K., et al. 2015, A&A, 577, A83. doi:10.1051/0004-6361/201424915
- Drkaćkowska, J., Bitsch, B., Lambrechts, M., et al. 2023, Protostars and Planets VII, 534, 717. doi:10.48550/arXiv.2203.09759
- Dressing, C. D. & Charbonneau, D. 2015, ApJ, 807, 45. doi:10.1088/0004-637X/807/1/45
- Ezzeddine, R., Frebel, A., & Plez, B. 2017, ApJ, 847, 142. doi:10.3847/1538-4357/aa8875
- Figueira, P., Pont, F., Mordasini, C., et al. 2009, A&A, 493, 671. doi:10.1051/0004-6361:20078951
- Fisher, C., Akin, C. J., Allen, N., et al. 2023, JWST Proposal. Cycle 2, 4195
- Follert, R., Dorn, R. J., Oliva, E., et al. 2014, Proc. SPIE, 9147, 914719. doi:10.1117/12.2054197
- Fukui, A., Narita, N., Kurosaki, K., et al. 2013, ApJ, 770, 95. doi:10.1088/0004-637X/770/2/95
- Gaia Collaboration 2022, VizieR Online Data Catalog, I/355. doi:10.26093/cds/vizier.1355
- Gaidos, E., Haghhipour, N., Agol, E., et al. 2007, Science, 318, 210. doi:10.1126/science.1144358
- Giacalone, S., Dressing, C. D., Hedges, C., et al. 2022, AJ, 163, 99. doi:10.3847/1538-3881/ac4334
- Gillon, M., Pont, F., Demory, B.-O., et al. 2007, A&A, 472, L13. doi:10.1051/0004-6361:20077799
- Greene, T. P., Beatty, T. G., Rieke, M. J., et al. 2017, JWST Proposal. Cycle 1, 1185
- Greene, T. P., Lagage, P.-O., Rieke, M. J., et al. 2017, JWST Proposal. Cycle 1, 1177
- Gustafsson, B., Edvardsson, B., Eriksson, K., et al. 2008, A&A, 486, 951. doi:10.1051/0004-6361:200809724
- Hejazi, N., Crossfield, I. J. M., Nordlander, T., et al. 2023, ApJ, 949, 79. doi:10.3847/1538-4357/acccb97
- Henry, T. J., Jao, W.-C., Winters, J. G., et al. 2018, AJ, 155, 265. doi:10.3847/1538-3881/aac262
- Hirano, T., Livingston, J. H., Fukui, A., et al. 2021, AJ, 162, 161. doi:10.3847/1538-3881/ac0fd
- Holtzman, J. A., Hasselquist, S., Shetrone, M., et al. 2018, AJ, 156, 125. doi:10.3847/1538-3881/aad4f9
- Hunter, J. D. 2007, Computing in Science and Engineering, 9, 90. doi:10.1109/MCSE.2007.55
- Husser, T.-O., Wende-von Berg, S., Dreizler, S., et al. 2013, A&A, 553, A6. doi:10.1051/0004-6361/201219058
- Ishikawa, H. T., Aoki, W., Hirano, T., et al. 2022, AJ, 163, 72. doi:10.3847/1538-3881/ac3ee0
- Ishikawa, H. T., Aoki, W., Kotani, T., et al. 2020, PASJ, 72, 102. doi:10.1093/pasj/psaa101
- Jofré, P., Heiter, U., & Soubiran, C. 2019, ARA&A, 57, 571. doi:10.1146/annurev-astro-091918-104509
- Kolecki, J. R. & Wang, J. 2022, AJ, 164, 87. doi:10.3847/1538-3881/ac7de3
- Kollmeier, J. A., Zasowski, G., Rix, H.-W., et al. 2017, arXiv:1711.03234. doi:10.48550/arXiv.1711.03234
- Kosiarek, M. R., Crossfield, I. J. M., Hardegree-Ullman, K. K., et al. 2019, AJ, 157, 97. doi:10.3847/1538-3881/aaf79c
- Kraus, A. L. & Hillenbrand, L. A. 2007, AJ, 134, 2340. doi:10.1086/522831
- Lanotte, A. A., Gillon, M., Demory, B.-O., et al. 2014, A&A, 572, A73. doi:10.1051/0004-6361/201424373
- Lind, K., Amarsi, A. M., Asplund, M., et al. 2017, MNRAS, 468, 4311. doi:10.1093/mnras/stx673
- Lissauer, J. J. & de Pater, I. 2013, Fundamental Planetary Science, by Jack J. Lissauer , Imke de Pater, Cambridge, UK: Cambridge University Press, 2013
- Luque, R., Bean, J. L., Changeat, Q., et al. 2023, JWST Proposal. Cycle 2, 3263
- Luque, R. & Pallé, E. 2022, Science, 377, 1211. doi:10.1126/science.abl7164
- Lustig-Yaeger, J., Fu, G., May, E. M., et al. 2023, Nature Astronomy, 7, 1317. doi:10.1038/s41550-023-02064-z
- Maciejewski, G., Niedzielski, A., Nowak, G., et al. 2014, AcA, 64, 323. doi:10.48550/arXiv.1501.02711
- Madhusudhan, N. 2012, ApJ, 758, 36. doi:10.1088/0004-637X/758/1/36
- Majewski, S. R., Schiavon, R. P., Frinchaboy, P. M., et al. 2017, AJ, 154, 94. doi:10.3847/1538-3881/aa784d
- Maldonado, J., Micela, G., Baratella, M., et al. 2020, A&A, 644, A68. doi:10.1051/0004-6361/202039478
- Mamajek, E. E., Prsa, A., Torres, G., et al. 2015, arXiv:1510.07674. doi:10.48550/arXiv.1510.07674
- Mann, A. W., Feiden, G. A., Gaidos, E., et al. 2015, ApJ, 804, 64. doi:10.1088/0004-637X/804/1/64
- Mashonkina, L., Jablonka, P., Sitnova, T., et al. 2017, A&A, 608, A89. doi:10.1051/0004-6361/201731582
- Masseron, T., Merle, T., & Hawkins, K. 2016, Astrophysics Source Code Library. ascl:1605.004

- May, E. M., MacDonald, R. J., Bennett, K. A., et al. 2023, *ApJL*, 959, L9. doi:10.3847/2041-8213/ad054f
- Mikolaitis, Š., de Laverny, P., Recio-Blanco, A., et al. 2017, *A&A*, 600, A22. doi:10.1051/0004-6361/201629629
- Miller, G. E. & Scalo, J. M. 1979, *ApJS*, 41, 513. doi:10.1086/190629
- Morello, G., Parviainen, H., Murgas, F., et al. 2023, *A&A*, 673, A32. doi:10.1051/0004-6361/202243592
- Morley, C. V., Knutson, H., Line, M., et al. 2017, *AJ*, 153, 86. doi:10.3847/1538-3881/153/2/86
- Moses, J. I., Line, M. R., Visscher, C., et al. 2013, *ApJ*, 777, 34. doi:10.1088/0004-637X/777/1/34
- Mucciarelli, A., Pancino, E., Lovisi, L., et al. 2013, *ApJ*, 766, 78. doi:10.1088/0004-637X/766/2/78
- Nascimbeni, V., Piotto, G., Pagano, I., et al. 2013, *A&A*, 559, A32. doi:10.1051/0004-6361/201321971
- Newton, E. R., Charbonneau, D., Irwin, J., et al. 2015, *ApJ*, 800, 85. doi:10.1088/0004-637X/800/2/85
- Nissen, P. E. 2013, *A&A*, 552, A73. doi:10.1051/0004-6361/201321234
- Nortmann, L., Pallé, E., Salz, M., et al. 2018, *Science*, 362, 1388. doi:10.1126/science.aat5348
- Pacetti, E., Turrini, D., Schisano, E., et al. 2022, *ApJ*, 937, 36. doi:10.3847/1538-4357/ac8b11
- Passegger, V. M., Reiners, A., Jeffers, S. V., et al. 2018, *A&A*, 615, A6. doi:10.1051/0004-6361/201732312
- Passegger, V. M., Schweitzer, A., Shulyak, D., et al. 2019, *A&A*, 627, A161. doi:10.1051/0004-6361/201935679
- Pelletier, S., Benneke, B., Darveau-Bernier, A., et al. 2021, *AJ*, 162, 73. doi:10.3847/1538-3881/ac0428
- Plez, B. 2012, Astrophysics Source Code Library. ascl:1205.004
- Polanski, A. S., Crossfield, I. J. M., Howard, A. W., et al. 2022, *Research Notes of the American Astronomical Society*, 6, 155. doi:10.3847/2515-5172/ac8676
- Quirrenbach, A., Amado, P. J., Seifert, W., et al. 2012, *Proc. SPIE*, 8446, 84460R. doi:10.1117/12.925164
- Reiners, A., Zechmeister, M., Caballero, J. A., et al. 2018, *A&A*, 612, A49. doi:10.1051/0004-6361/201732054
- Ribas, I., Reiners, A., Zechmeister, M., et al. 2023, *A&A*, 670, A139. doi:10.1051/0004-6361/202244879
- Ricker, G. R., Winn, J. N., Vanderspek, R., et al. 2015, *Journal of Astronomical Telescopes, Instruments, and Systems*, 1, 014003. doi:10.1117/1.JATIS.1.1.014003
- Roederer, I. U., Preston, G. W., Thompson, I. B., et al. 2014, *AJ*, 147, 136. doi:10.1088/0004-6256/147/6/136
- Rojas-Ayala, B., Covey, K. R., Muirhead, P. S., et al. 2012, *ApJ*, 748, 93. doi:10.1088/0004-637X/748/2/93
- Rosenthal, L. J., Fulton, B. J., Hirsch, L. A., et al. 2021, *ApJS*, 255, 8. doi:10.3847/1538-4365/abe23c
- Salpeter, E. E. 1955, *ApJ*, 121, 161. doi:10.1086/145971
- Salz, M., Czesla, S., Schneider, P. C., et al. 2018, *A&A*, 620, A97. doi:10.1051/0004-6361/201833694
- Salz, M., Schneider, P. C., Czesla, S., et al. 2015, *A&A*, 576, A42. doi:10.1051/0004-6361/201425243
- Sánchez-López, A., Alonso-Floriano, F. J., López-Puertas, M., et al. 2019, *A&A*, 630, A53. doi:10.1051/0004-6361/201936084
- Santos, N. C., Adibekyan, V., Dorn, C., et al. 2017, *A&A*, 608, A94. doi:10.1051/0004-6361/201731359
- Sarmiento, P., Rojas-Ayala, B., Delgado Mena, E., et al. 2021, *A&A*, 649, A147. doi:10.1051/0004-6361/202039703
- Schneider, A. D. & Bitsch, B. 2021, *A&A*, 654, A72. doi:10.1051/0004-6361/202141096
- Schweitzer, A., Passegger, V. M., Cifuentes, C., et al. 2019, *A&A*, 625, A68. doi:10.1051/0004-6361/201834965
- Shields, A. L., Ballard, S., & Johnson, J. A. 2016, *PhR*, 663, 1. doi:10.1016/j.physrep.2016.10.003
- Simonian, G. V. A., Pinsonneault, M. H., Terndrup, D. M., et al. 2020, *ApJ*, 898, 76. doi:10.3847/1538-4357/ab9a43
- Smith, V. V., Bizyaev, D., Cunha, K., et al. 2021, *AJ*, 161, 254. doi:10.3847/1538-3881/abefdc
- Souto, D., Cunha, K., García-Hernández, D. A., et al. 2017, *ApJ*, 835, 239. doi:10.3847/1538-4357/835/2/239
- Souto, D., Cunha, K., & Smith, V. V. 2021, *ApJ*, 917, 11. doi:10.3847/1538-4357/abfdb5
- Souto, D., Cunha, K., Smith, V. V., et al. 2020, *ApJ*, 890, 133. doi:10.3847/1538-4357/ab6d07
- Souto, D., Cunha, K., Smith, V. V., et al. 2022, *ApJ*, 927, 123. doi:10.3847/1538-4357/ac4891
- Souto, D., Cunha, K., Smith, V. V., et al. 2016, *ApJ*, 830, 35. doi:10.3847/0004-637X/830/1/35
- Souto, D., Unterborn, C. T., Smith, V. V., et al. 2018, *ApJL*, 860, L15. doi:10.3847/2041-8213/aac896
- Stassun, K. G., Oelkers, R. J., Paegert, M., et al. 2019, *AJ*, 158, 138. doi:10.3847/1538-3881/ab3467
- Stevenson, K. B., Harrington, J., Nymeyer, S., et al. 2010, *Nature*, 464, 1161. doi:10.1038/nature09013
- Teske, J. K., Cunha, K., Smith, V. V., et al. 2014, *ApJ*, 788, 39. doi:10.1088/0004-637X/788/1/39
- Thiabaud, A., Marboeuf, U., Alibert, Y., et al. 2015, *A&A*, 580, A30. doi:10.1051/0004-6361/201525963
- Torres, G., Winn, J. N., & Holman, M. J. 2008, *ApJ*, 677, 1324. doi:10.1086/529429
- Tsuji, T., Nakajima, T., & Takeda, Y. 2015, *PASJ*, 67, 26. doi:10.1093/pasj/psu160
- Turner, J. D., Pearson, K. A., Biddle, L. I., et al. 2016, *MNRAS*, 459, 789. doi:10.1093/mnras/stw574
- Unterborn, C. T. & Panero, W. R. 2017, *ApJ*, 845, 61. doi:10.3847/1538-4357/aa7f79

- van der Walt, S., Colbert, S. C., & Varoquaux, G. 2011, Computing in Science and Engineering, 13, 22. doi:10.1109/MCSE.2011.37
- Wanderley, F., Cunha, K., Souto, D., et al. 2023, ApJ, 951, 90. doi:10.3847/1538-4357/acd4bd
- Wilson, R. F., Teske, J., Majewski, S. R., et al. 2018, AJ, 155, 68. doi:10.3847/1538-3881/aa9f27
- Yee, S. W., Petigura, E. A., & von Braun, K. 2017, ApJ, 836, 77. doi:10.3847/1538-4357/836/1/77
- Zeng, L., Sasselov, D. D., & Jacobsen, S. B. 2016, ApJ, 819, 127. doi:10.3847/0004-637X/819/2/127
- Zhang, M., Bean, J. L., Hu, R., et al. 2023, JWST Proposal. Cycle 2, 3784